Engineering Journal

American Institute of Steel Construction

Fourth Quarter 2018 Volume 55, No. 4

www.aisc.org

Engineering Journal

American Institute of Steel Construction

Dedicated to the development and improvement of steel construction, through the interchange of ideas, experiences and data.

Editorial Staff

Editor	**Margaret A. Matthew, P.E.**
Managing Editor	**Keith A. Grubb, S.E., P.E.**
Research Editor	**Judy Liu, Ph.D.**
Production Editor	**Erika Salisbury**

Officers

David Zalesne
Chairman

Jack Klimp
Vice Chairman

David B. Ratterman
Secretary & General Counsel

Charles J. Carter, S.E., P.E., Ph.D.
President

Scott L. Melnick
Senior Vice President

Lawrence F. Kruth, P.E.
Vice President

Tabitha S. Stine, S.E., P.E.
Vice President

Mark W. Trimble, P.E.
Vice President

The articles contained herein are not intended to represent official attitudes, recommendations or policies of the Institute. The Institute is not responsible for any statements made or opinions expressed by contributors to this Journal.

The opinions of the authors herein do not represent an official position of the Institute, and in every case the officially adopted publications of the Institute will control and supersede any suggestions or modifications contained in any articles herein.

The information presented herein is based on recognized engineering principles and is for general information only. While it is believed to be accurate, this information should not be applied to any specific application without competent professional examination and verification by a licensed professional engineer. Anyone making use of this information assumes all liability arising from such use.

Manuscripts are welcomed, but publication cannot be guaranteed. All manuscripts should be submitted in duplicate. Authors do not receive a remuneration. Guidelines for authors are printed on the inside back cover.

Engineering Journal (ISSN 0013-8029) is published quarterly. Subscriptions: Members: one subscription, $40 per year, included in dues; Additional Member Subscriptions: $40 per year. Non-Members U.S.: $160 per year. Foreign (Canada and Mexico): Members $80 per year. Non-Members $160 per year. Published by the American Institute of Steel Construction at 130 E. Randolph Street, Suite 2000, Chicago, IL 60601.

Periodicals postage paid at Chicago, IL and additional mailing offices. **Postmaster:** Send address changes to *Engineering Journal* in care of the American Institute of Steel Construction, 130 E. Randolph Street, Suite 2000, Chicago, IL 60601.

Copyright 2018 by the American Institute of Steel Construction. All rights reserved. No part of this publication may be reproduced without written permission. The AISC logo is a registered trademark of AISC.

Subscriptions: subscriptions@aisc.org, 312.670.2400

Archives: Search at **www.aisc.org/ej**. Article downloads are free for current members and are avaialable for a nominal fee for non-members.

Technical Note

Post-Fire Axial Load Resistance of Concrete-Filled, Double-Skin Tube (CFDST) Stub Columns

REZA IMANI and MICHEL BRUNEAU

ABSTRACT

This technical note reports findings on a series of squash tests to investigate the effects of a significant fire loading history on the axial load strength of concrete-filled, double-skin tube (CFDST) stub columns. Axial loading tests were conducted on two stub columns that were previously subjected to the first 60 minutes of the standard ASTM E119 (ASTM, 2012) fire. Results were compared to the resistance of an identical virgin stub column. Comparisons indicated an average reduction of 28% in the axial load strength of stub columns when subjected to the mentioned fire loading history.

Keywords: steel tube column, fire loading, ASTM E119, double skin, axial strength.

INTRODUCTION

Concrete-filled, double-skin tube (CFDST) columns have been shown to perform well under both single- and multi-hazard conditions (e.g., when subjected to inelastic cycling loads to simulate seismic effects, when subjected to blasts, and when subjected to subsequent cyclic and fire loading to simulate cascading effects—or fire and cyclic loading to simulate earthquakes happening on a building subjected to a fire years earlier) in several past studies (Zhao and Grzebieta, 2002; Han et al., 2004; Yang and Han, 2008; Lu et al., 2010; Fouche and Bruneau, 2010; Imani et al., 2014a; 2015). This has made CFDST columns appealing from a multi-hazard perspective. However, one specific aspect that needed to be considered in the referenced studies investigating the resilience of CFDST columns was whether the squash strength of CFDST columns was adequate solely from a post-fire perspective because any permanent effects from a prior fire loading would need to be known to ensure proper functioning of these columns through the life of a structure after exposure to a fire (as one of many limit states that may need to be evaluated in post-fire conditions to determine if repair or replacement is warranted). For that reason, this study examines the post-fire axial load resistance of CFDST stub columns following exposure to a standard ASTM E119 fire (ASTM, 2012). In addition, and to a lesser extent, fire test results were used to study the effect of ventilation holes on temperature distribution and concrete moisture content loss in CFDST stub columns.

SPECIMENS

Three CFDST stub columns, hereafter referred to as SC1, SC2 and SC3, were built with identical height (i.e., 1 ft) and cross-section, as shown in Figure 1. The outer and inner tubes were 8-in.- and 5-in.-diameter, respectively. Concrete was poured between the two steel tubes and, as recommended in AISC Design Guide 19 *Fire Resistance of Structural Steel Framing* (Ruddy et al., 2003), small (⅛-in.) vent holes were drilled into the outer tube to allow pressure relief during fire. Stub columns SC1 and SC2 were built with a total of two and three ventilation holes. The first two holes were located on the round surface of the specimens at about 1 in. from the top and bottom plates. The third hole, in the case of SC2, was located at the opposite side of the other vent hole drilled near the top end. The intent of an additional hole was to crudely investigate whether additional ventilation and pressure relief can change the resulting temperature history and possible permanent fire effects on the strength of stub columns. Stub column SC3 was kept without holes and was to be tested without having been previously exposed to fire to serve as a reference specimen.

FIRE TESTS

Stub columns SC1 and SC2 were subjected to the first 60 minutes of the ASTM E119 (ASTM, 2012) fire curve in a natural gas furnace. No insulation was used at the top or bottom ends of the specimens. The standard curve and fire

---

Reza Imani, Ph.D., P.E., Project Engineer, Thornton Tomasetti, San Francisco, CA. Email: RImani@thorntontomasetti.com (corresponding)

Michel Bruneau, Ph.D., P.Eng., Professor, Department of CSEE, University at Buffalo, Amherst, NY. Email: bruneau@buffalo.edu

Paper No. 2016-08R

duration were selected to provide a common comparison base for different specimens in this study as well as similar past studies. Three thermocouples located at mid-height of stub columns were monitoring temperature variations at three different points through the cross-section (i.e., inner surface of the outer tube, half-width through concrete, and outer surface of the inner tube) for both stub columns. A hole was drilled on the outer tube at this location to allow for the exit of wires. Figure 2 shows SC1 and SC2 after the fire test. No axial load was applied to the specimens during the fire test, but based on results for corresponding slender columns tested simultaneously (Imani et al., 2014a), it is known that these stub columns would not have reached their compression limit state. No visible damage was detected on the stub columns after the fire test for the intensity and duration described earlier. Both specimens were left to gradually cool down to room temperature.

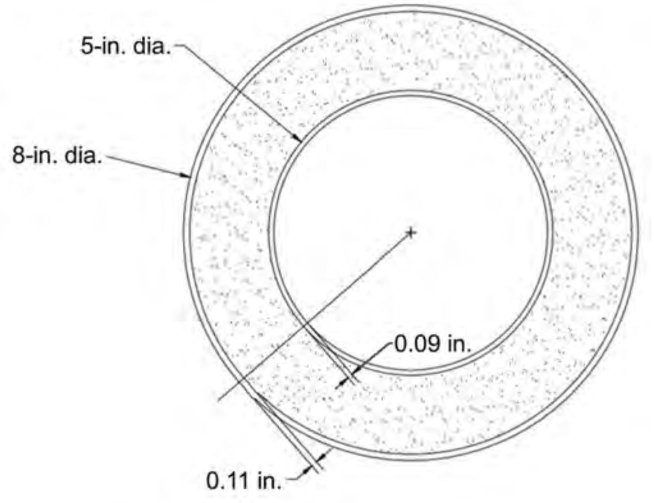

Fig. 1. Cross-section of the stub columns.

Figure 3 shows the time histories of temperature recorded by the thermocouples installed in the stub columns along with the average furnace air temperature during fire. Note that the actual test stopped at around 70 minutes and the recorders were kept operating for a few additional minutes. The recorded temperature curves generally show a smooth increasing trend, except for the ones recorded by the thermocouples installed on the surface of the inner tube for both SC1 and SC2 that show sudden fluctuations, especially during the first 20 minutes of the test. These fluctuations are speculated to occur due to the random arrangement of aggregates in the concrete of the specimens, causing moisture and pressure relief at certain times and affecting the thermocouple readings.

Comparison of temperature time histories for the two stub columns show that the temperature values for all of the three

(a) (b)

Fig. 2. Stub columns after fire test: (a) SC1; (b) SC2.

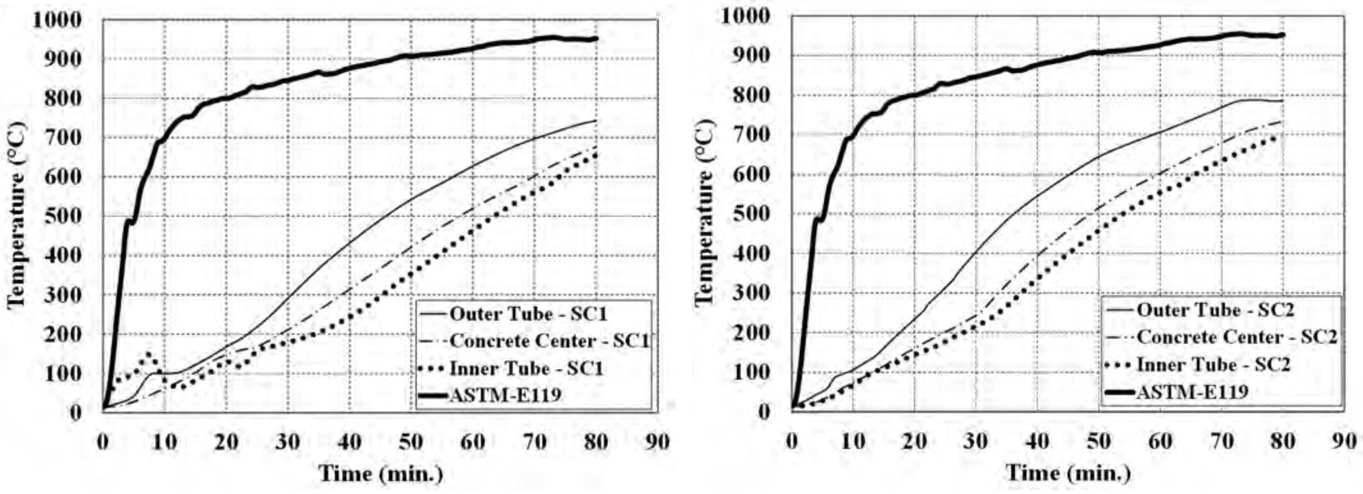

(a) (b)

Fig. 3. Temperature data measured from the stub columns: (a) SC1; (b) SC2.

thermocouples installed in SC2 are about 50°C higher than the values for SC1. Because the difference in temperature is noticeable in values recorded on the outer surfaces of columns and from the beginning stages of the test, it is inferred that the reason for this difference is likely related to the different locations of the stub columns at the bottom of the furnace. Note that nine thermocouples were installed at different heights inside the furnace, and the average of readings from all of those was used to control average temperature to follow the standard fire curve. Beyond this, recommended additional experimental research may be informative to study the possible effect of vent holes on temperature distribution within the specimens.

Stub columns were also used to study the effects of fire tests on the moisture content of concrete by comparing the measured relative humidity (RH) of the two stub columns tested in the fire (i.e., SC1 and SC2) with that of the third one, SC3, which was kept intact in the lab. Relative humidity is the amount of water vapor present in a volume of air at a given temperature compared to the maximum amount that the air could hold at that temperature, expressed as a percentage. Relative humidity of the three stub columns were measured based on the standard ASTM F2170 (ASTM, 2011). An electronic probe was inserted into holes drilled into the concrete (after running through the steel) to measure the RH values. Measurements gave post-fire RH values of 29% and 20% for SC1 and SC2, respectively. These values were about half of the RH value of 59% for SC3, which wasn't subjected to the fire test (RH was measured about 6 months after casting). Relative humidity of 59% is within the range of 50 to 75% defined by ASTM E119 (ASTM, 2012) for concrete dried at room temperature. The effect of the additional vent hole is seen in the difference of RH values for SC1 and SC2. Note that the holes required for the RH tests were drilled after the fire tests at locations, which were not close to the original vent holes of stub columns to avoid capturing local effects.

SQUASH LOADING TEST

To investigate the permanent effects of an approximate 1-hour-long fire exposure on the squash load of CFDST columns (ASTM, 2012), an axial loading test was conducted on the SC1, SC2 and SC3 stub columns. The squash tests were conducted using the 2,200,000-lb uniaxial loading testing facility of Taylor Devices Inc. in Buffalo, New York. Axial load was applied to 12×12×¼-in. cap plates welded to both ends of each stub column. All tests were terminated upon observance of significant loss in axial load capacity, which was typically accompanied by severe local buckling of the steel. Figure 4 shows photos of all three failed stub columns.

Figure 5 shows axial load versus axial contraction results for all three stub columns (SC1, SC2 and SC3). The initial phase of all three curves (i.e., axial contraction below 0.025 in.) nearly follows a similar path, suggesting that the fire loading history, in the absence of structural loads, has caused no significant permanent effects on the elastic stiffness of SC1 and SC2.

However, the figure demonstrates differences in maximum strength and post-maximum strength for the three specimens. Stub columns SC1 and SC2, which were both subjected to fire previously, had maximum axial load values of 334 and 339 kips, respectively. These values are about 28% less than the 471-kip squash load obtained for the reference specimen not subjected to fire (SC3).

Cylinder tests showed an average f'_c of 9.7 ksi for concrete (normal weight, density: 150 pcf) from the specimen that was not tested in fire. Steel tubes were manufactured from ASTM A513 (ASTM, 2015) type 1 steel with nominal yield and tensile strength values of 32 ksi and 45 ksi, respectively. Steel coupon tests resulted in an average f_y of 50 ksi for the outer tube and 44 ksi for the inner tube (Imani et al., 2014b). The theoretical squash load can be calculated as:

$$f_y(A_{st,inner} + A_{st,outer}) + 0.85 f'_c A_{concrete} \tag{1}$$


(a) (b) (c)

Fig. 4. Failed stub columns: (a) SC1; (b) SC2; (c) SC3.

where A refers to the cross-sectional area described by the subscripts (i.e., inner/outer steel tubes and concrete between them) and f_y is the yield strength of steel taken from the coupon tests. Applying Equation 1 to the CFDST section geometry shown in Figure 1 with the room temperature values of f'_c and f_y (as previously mentioned) results in a theoretical squash load value of 428 kips. The theoretical calculated value is within 10% of the test result (i.e., 471 kips).

According to Eurocode 4 (CEN, 2005) specifications, the residual compressive strength of concrete heated to maximum temperature of θ_{max} and subsequently cooled down to ambient temperature of 20°C can be calculated as follows:

$$f'_{c,\theta max,20} = \phi f'_c$$

$$\phi = \begin{cases} k_{c,\theta max} & 20 \le \theta_{max} < 100 \\ 1.0 - \left[\dfrac{0.235(\theta_{max} - 100)}{200}\right] & 100 \le \theta_{max} < 300 \\ 0.9 k_{c,\theta max} & \theta_{max} \ge 300 \end{cases} \tag{2}$$

where $k_{c,\theta max}$ is a reduction factor that is provided in Eurocode 4 tables for normal- and light-weight concrete and f'_c refers to the compressive strength of concrete at room temperature. Considering $\theta_{max} \approx 700°C$ for the case in hand (see Figure 3) and a $k_{c,\theta max}$ factor of 0.3 (from Eurocode 4 tabulated values), the residual compressive strength is calculated to be about 27% of the initial (i.e., room temperature) f'_c value. For steel, although it is considered to almost fully recover after cooling down to room temperatures from maximum temperature levels seen in Figure 3, Eurocode conservatively recommends a 10% reduction factor to be applied to the room temperature yield strength value.

Using the residual values of strength for steel and concrete calculated with the average measured strength values at room temperature and the reduction factors mentioned earlier for the case in hand, a theoretical reduction of 40% is achieved for the squash load of stub columns. As such, test results reveal that the strength reduction factors specified in Eurocode 4 might be slightly conservative (28% reduction in test versus the calculated 40%) but can provide a reasonable estimate of the post-fire conditions. A similar reduction is seen in the post-peak strength plateau reached in both SC1 and SC2 curves, where SC1 and SC2, respectively, show 18 and 24% reductions in axial force from the recorded value of 305 kips for SC3 (i.e., the specimen not subjected to fire).

CONCLUSION

Experimental observations presented in this study indicated that a fire loading history, albeit causing no significant visible damage, can induce permanent effects on structural integrity of CFDST stub columns. More specifically, an average 28% reduction was observed in the axial squash load strength of two stub columns previously exposed to a fire loading history as opposed to a reference specimen not subjected to fire. Moreover, a simple comparison between two specimens with different number of vent holes demonstrated that more ventilation accelerates concrete moisture loss without significantly affecting the temperature distribution during fire. However, more research is needed to further validate this observation.

ACKNOWLEDGMENTS

This study was supported by MCEER, University at Buffalo. The authors also would like to thank Mr. Douglas P. Taylor and staff at Taylor Devices Inc. for their help and support on the squash loading tests.

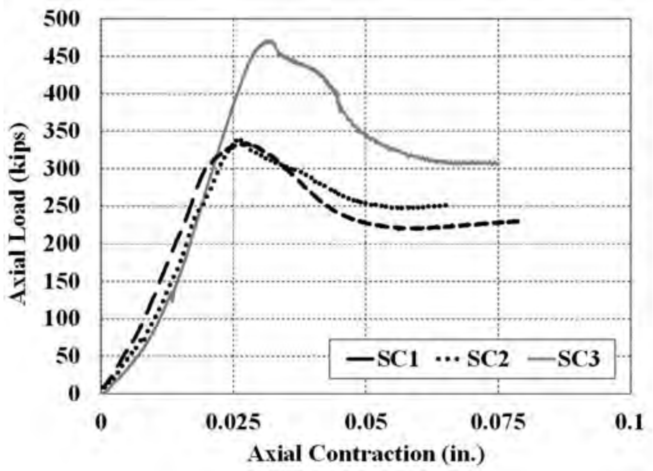

Fig. 5. Axial force vs. axial contraction curves from squash tests.

REFERENCES

ASTM (2011), "Standard Test Method for Determining Relative Humidity in Concrete Floor Slabs Using in Situ Probes," ASTM F2170-11, American Society for Testing and Materials, West Conshohocken, PA.

ASTM (2012), "Standard Test Methods for Fire Tests of Building Construction and Materials," ASTM E119-12a, American Society for Testing and Materials, West Conshohocken, PA.

ASTM (2015), "Standard Specification for Electric-Resistance-Welded Carbon and Alloy Steel Mechanical Tubing," ASTM A513/A513M-15, American Society for Testing and Materials, West Conshohocken, PA.

CEN (2005), "Eurocode 4: Design of Composite Steel and Concrete Structures, Part 1.2: General Rules—Structural Fire Design," Comité Européen de Normalisation, Brussels, Belgium.

Fouche, P. and Bruneau, M. (2010), "Non-Linear Analysis of Multi-Hazard Performance of Concrete Filled Steel Tubes Bridge Piers," 8th International Conference on Short and Medium Span Bridges, Niagara Falls, Ontario, Canada.

Han, L.H., Tao, Z., Huang, H. and Zhao, X.L. (2004), "Concrete-Filled Double Skin (SHS Outer and CHS Inner) Steel Tubular Beam-Columns," *Thin Wall Structures,* Vol. 42, No. 9, pp. 1,329–1,355.

Imani, R., Mosqueda, G. and Bruneau, M. (2014a), "Experimental Study on Post-Earthquake Fire Resistance of Ductile Concrete-Filled Double-Skin Tube Columns," *Journal of Structural Engineering,* ASCE, doi: 10.1061/(ASCE)ST.1943-541X.0001168, 04014192.

Imani, R., Mosqueda, G. and Bruneau, M. (2014b), "Post-Earthquake Fire Resistance of Ductile Concrete-Filled Double-Skin Tube Columns," MCEER Technical Report MCEER-14-0008, Buffalo, NY, http://mceer.buffalo.edu/publications/catalog/reports/Post-Earthquake-Fire-Resistance-of-Ductile-Concrete-Filled-Double-Skin-Tube-Columns-MCEER-14-0008.html.

Imani, R., Mosqueda, G. and Bruneau, M. (2015), "Finite Element Simulation of Concrete Filled Double-Skin Tube Columns Subjected to Post-Earthquake Fires," *Journal of Structural Engineering,* ASCE, doi: 10.1061/(ASCE)ST.1943-541X.0001301.

Lu, H., Han, L.H. and Zhao, X.L. (2010), "Fire Performance of Self-Consolidating Concrete Filled Double Skin Steel Tubular Columns: Experiments," *Fire Safety Journal,* Vol. 45, No. 2, pp. 106–115.

Ruddy, J.L., Marlo, J.P., Ioannides, S.A. and Alfawakhiri, F. (2003), *Fire Resistance of Structural Steel Framing*, Design Guide 19, American Institute of Steel Construction, Chicago, IL.

Yang, Y.F. and Han, L.H. (2008), "Concrete-Filled Double-Skin Tubular Columns under Fire," *Magazine of Concrete Research,* Vol. 60, No. 3, pp. 211–222.

Zhao, X.L. and Grzebieta, R. (2002), "Strength and Ductility of Concrete Filled Double Skin (SHS Inner and SHS Outer) Tubes," *Thin Wall Structures,* Vol. 40, No. 2, pp. 199–213.

Quantifying Inelastic Force and Deformation Demands on Buckling Restrained Braces and Structural System Response

JUSTIN D. MARSHALL, BRANDT SAXEY and ZHONGLIANG XIE

ABSTRACT

Buckling-restrained braced frames (BRBF) have become a very popular lateral-resisting system due to their balanced, full hysteresis and the ability to tailor stiffness, within limits, and strength to meet specific design requirements. This paper reports the results of an analytical investigation on the performance of buckling-restrained braces (BRB) and the global performance of BRBF with a focus on the ductility and overstrength demands on the braces. Nonlinear analytical models of various three- and six-story steel frames were subjected to a suite of earthquake records to determine the demands on the BRB elements and the overall frame response. The structure variations include the location (i.e., seismic hazard), seismic importance factor, I_e, brace configuration (chevron versus single diagonal), and BRB yielding core length. The analysis also investigates the ratio of the impact of an error in the approximation of the BRB elastic stiffness on the system performance.

Keywords: buckling-restrained brace, ductility in steel structures, overstrength demands, nonlinear analysis.

INTRODUCTION

Buckling-restrained braces (BRB) are an example of a recent innovation in structural engineering that has had a significant impact on design of steel structures. As opposed to conventional concentrically braced frames that yield in tension and buckle in compression, BRB have a full and essentially balanced hysteresis. This occurs because the flexural demands are taken by the buckling restraining element of the brace, which allows yielding in tension and compression of the core steel. Yielding in both directions allows for material limit states in both directions and a much greater capacity to dissipate energy than yielding and buckling of a concentric brace. In addition, the geometry of the yielding core plate can be tailored to the strength and stiffness requirements for a given application.

The typical configuration of BRB in U.S. practice today (see Figure 1) consists of a core plate with a yielding region that is tapered down from the connection regions at the end. The core plate is covered by a restraining tube that is filled with mortar to provide the restraining mechanism. Between the steel and mortar, an air gap or bond breaker is used to minimize axial load transfer between the core and the restraining system. Significant experimental and analytical research has investigated the performance of BRB. The original research conducted on a plate debonded from constraining concrete was conducted by Yoshino and Karino (1971) and Wakabayashi et al. (1973). Many researchers since then have investigated a myriad of different combinations of core plate and buckling restraining mechanisms (Xie, 2005; Uang et al., 2004). A significant amount of research has been done related to component testing of BRB; however, system-level research has been less common. A few examples of either experimental or analytical research on system level response include Fahnestock et al. (2006), Mahin et al. (2004), Sabelli (2001), Tsai and Hsiao (2008), and Chou et al. (2012).

One of the challenges in determining the proper ductility-based design requirements for a lateral resisting system is determining appropriate limitations within the code that enable design provisions that result in robust, safe structures. These limitations must then be linked to an elastic design procedure based on an elastic and static analysis model. Currently, BRB are designed and detailed in the United States in accordance with ASCE/SEI 7 (ASCE, 2010) and AISC/ANSI 341 (AISC, 2010a). The provisions that impact BRB design are the seismic performance factors (R, Ω_o, C_d) and the capacity design provisions, which include the tension (ω) and compression (β) strength adjustment factors. The seismic performance factors relate the elastic analysis model to the expected inelastic response. The capacity design requirements ensure that other structural elements in the load path have sufficient capacity for the maximum inelastic demand required of the BRB. The current requirement to determine

Justin D. Marshall, Associate Professor of Civil Engineering, Auburn University, Auburn, AL. Email: jdmarshall@auburn.edu (corresponding)

Brandt Saxey, Vice President Preconstruction Sales and Technical Director, CoreBrace, West Jordan, UT. Email: brandt.saxey@corebrace.com

Zhongliang Xie, Graduate Research Assistant, School of Civil and Construction Engineering, Oregon State University, Corvallis, OR. Email: xiezho@onid.oregonstate.edu

Paper No. 2017-18

the brace forces at the expected deformations requires a drift that is the larger value of 2% of the story height or twice the design story drift. The difficulty with this calculation is that the overstrength (the maximum expected brace force) depends on the geometry of the frame, which can require multiple iterations as section sizes change.

The research aim is to add to the data available on system-level response of BRB. A three-story and a six-story structure, which were previously used for research on braced frames (Sabelli, 2001) and are based on the SAC Steel Project buildings (FEMA, 2000), have been used in this research. The varied parameters include seismic hazard, brace configuration, seismic importance factor (I_e), and yielding core length. Two different seismic hazards—Los Angeles and Riverside, California—are utilized. Both are in the highest seismic design category, but there is a significant difference in the spectral accelerations. Single-diagonal and chevron (inverted-V) configurations are used to evaluate how the yielding core length difference and a reduced number of braces affect performance. The seismic importance factor is investigated by designing the BRB for a normal and critical occupancy structure ($I_e = 1$ and $I_e = 1.5$). Lastly, one of the concerns associated with tailoring BRB for increased stiffness is the impact of a shortened yielding core. Two core lengths using the same cross-sectional area are analyzed to study the impact of excessively short yield lengths. The first yielding core length was associated with the minimal stiffness the brace would be designed for and is referred to as the normal yielding core length. The shorter yielding core length was associated with what was considered the effective maximum stiffness the BRB could achieve. This was established by shortening the yielding core length until a 2% story drift would produce a 3 to 3.5% core strain.

One other component of the study is looking at the importance of accurately modeling the initial stiffness of braces. For typical conventional braces, the brace stiffness is based on the section and the working point lengths. For BRB, significant efforts are made to better approximate the brace stiffness. Using some of the structures in this research, the elastic stiffness was modified by ±10% to determine the impact of initial elastic stiffness on global inelastic response.

STRUCTURE DESCRIPTIONS AND PARAMETERS

All versions of the three- and six-story structures were designed using the equivalent lateral force (ELF) procedure specified in ASCE 7 (2010). The design gravity loads are the same as those specified by Sabelli (2001). The live load for the structures is 50 psf. The structural system is a typical steel frame structure. The basic dead load including superimposed loads varies from about 84 to 89 psf, with the mechanical penthouse having a dead load assigned to the roof of 148 psf. The same gravity system, columns and beams are used for all the versions of the buildings. The only difference among the various building versions is the BRB. A yield stress of 38 ksi was assumed for all BRB designs to size the core areas. The two different seismic hazards used in the analyses are Riverside, CA ($S_{DS} = 1.0$, $S_{D1} = 0.6$), and Los Angeles, CA ($S_{DS} = 1.39$, $S_{D1} = 0.77$). Both locations are considered site class D. The Seismic Design Category for normal occupancy structures is D. For the structures designed with $I_e = 1.5$, the Seismic Design Category is E and F for Riverside and Los Angeles, respectively. In total, 20 building variations were designed; 10 for each height.

Table 1 shows the fundamental period of vibration and the maximum story-drift ratio for each of the 20 building configurations. The model nomenclature, which will be used throughout to identify the structures, is based on the various parameters of the various structures. Los Angeles (LA) and Riverside (Riv) and the number of stories (3 or 6) are the first component. The two letters after the hyphen indicate the brace configuration: either chevron (CH) or single diagonal (SD). The last portion indicates the parameters for increased importance ($I_e = 1.5$) or shortened-yield length (S). Where no final parameter exists following the brace configuration, it represents a normal yield length brace and normal risk category structure ($I_e = 1$). The modal information and maximum story-drift ratios provide information about the stiffness and the dynamics of the various configurations in the elastic realm. The limiting drift ratios for these structures are all within the allowable limit. A 2% drift ratio is the limit for all the structures, with the exception of the structures classified as Risk Category IV ($I_e = 1.5$),

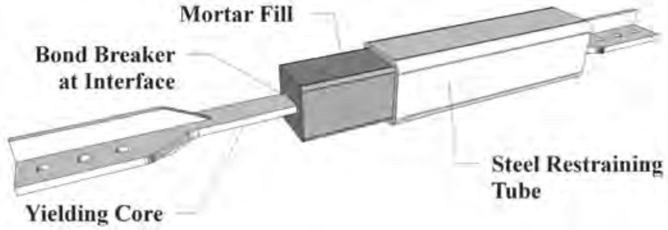

Fig. 1. Typical U.S. BRB configuration.

Table 1. Period of Vibration and Maximum Drift Ratio for Building Models

Model	Fundamental Period (sec)	Maximum Story-Drift Ratio	Model	Fundamental Period (sec)	Maximum Story-Drift Ratio
LA3-CH	0.52	0.0052	Riv3-CH	0.57	0.0057
LA3-CH1.5	0.45	0.0045	Riv3-CH1.5	0.49	0.0041
LA3-CHS	0.48	0.0051	Riv3-CHS	0.52	0.0046
LA3-SD	0.58	0.0097	Riv3-SD	0.64	0.0089
LA3-SDS	0.49	0.0079	Riv3-SDS	0.53	0.0069
LA6-CH	1.27	0.011	Riv6-CH	1.34	0.010
LA6-CH1.5	1.09	0.009	Riv6-CH1.5	1.18	0.008
LA6-CHS	1.10	0.009	Riv6-CHS	1.16	0.008
LA6-SD	1.44	0.017	Riv6-SD	1.61	0.015
LA6-SDS	1.23	0.014	Riv6-SDS	1.36	0.011

where the allowable drift ratio is 1%. While this information is very valuable for elastic response, the variation in the response of the structure under a nonlinear response history analysis can vary significantly for structures with similar elastic behavior.

Three-Story Structure

The three-story structure is a typical office building with 13-ft story heights. The plan dimensions are 124 ft × 184 ft with 30-ft-square structural bays. The building envelope is 2 ft outside the structural gridlines on all sides. All the braced frames are at the building perimeter. Two bays of bracing are present on each building face. A building elevation and plan are shown in Figure 2. The column and beam sizes are consistent for all the different configurations. Figure 2 shows the chevron bracing in solid lines and the single-diagonal configuration in dashed lines. Table 2 provides details about the BRB elements in all variations of the three-story structures. The yield length ratio is defined as the ratio of the yielding core length to the working point length of the braces.

Six-Story Structure

The six-story structure is also a typical office building. The first story height is 18 ft with the remaining stories having a 13-ft height. The building is square in plan (154 ft) with 30-ft-square bays. The building envelope is 2 ft outside the structural grid. Figure 3 shows an elevation view, and Figure 4 shows a plan view of the six-story structure. Three bays of perimeter bracing are used on each face of the building. Figure 3 shows the chevron bracing in solid lines and the single-diagonal configuration in dashed lines. The fundamental period of vibration and the design story drift for the different configurations of the six-story structure are presented in Table 1. Table 3 shows details about the BRB properties used in the different six-story models. The naming convention for the analysis models is the same as described for the three-story structure.

MODELING AND ANALYSIS

The building designs were completed using SAP 2000 version 15 (CSI, 2013). The nonlinear dynamic analysis was completed in Perform 3D version 5 (CSI, 2011). As is shown in Figures 2 and 3, a planar frame model is used for the analyses. In order to capture P-delta effects, a leaning P-delta column is used. The P-delta column captures the gravity loading and the continuous column effect of the leaning columns. It is a nonstandard column shape with the moment of inertia equal to the sum of the weak-axis properties of the tributary columns. An equal displacement constraint is used at each floor to constrain the P-delta column to the frame. Gravity loads are applied to the model as both point and distributed loads. Distributed loads are used on the beams except where those loads would induce gravity loads into the BRB in the chevron configuration. In this case, the tributary gravity loads were applied directly to the column. Dead load and 50% of live load are applied to the frame before the earthquake analysis. Tributary horizontal joint masses are applied at all the nodes in the model.

Beams in the unbraced bays are modeled as elastic beam elements. Beams in the braced bays, specifically for the chevron configurations, were modeled as inelastic beams based on the potential for plastic deformations due to unbalanced brace forces. A yield stress of 50 ksi was used for the beam elements. All beam column connections were assumed to be pinned connections because it is expected that a simple connection would be used adjacent to the gusset plate to allow for rotation between the beam and column

Table 2. BRB Properties for Three-Story Building Models

Model	Story Level	Yield Force (kips)	Yield Length (in.)	Yield Length Ratio	Model	Story Level	Yield Force (kips)	Yield Length (in.)	Yield Length Ratio
LA3-CH	3rd	161.5	152.9	0.64	Riv3-CH	3rd	123.5	158.1	0.66
	2nd	247.0	138.5	0.58		2nd	209.0	148.6	0.62
	1st	304.0	131.9	0.55		1st	228.0	138.1	0.58
LA3-CH1.5	3rd	247.0	138.5	0.58	Riv3-CH1.5	3rd	190.0	151.7	0.64
	2nd	380.0	130.1	0.55		2nd	304.0	133.2	0.56
	1st	437.0	127.3	0.53		1st	342.0	130.7	0.55
LA3-CHS	3rd	161.5	67.2	0.28	Riv3-CHS	3rd	123.5	66.6	0.28
	2nd	247.0	66.6	0.28		2nd	209.0	66.9	0.28
	1st	304.0	65.3	0.27		1st	228.0	65.0	0.27
LA3-SD	3rd	266.0	270.1	0.69	Riv3-SD	3rd	209.0	278.4	0.71
	2nd	418.0	258.3	0.66		2nd	342.0	261.8	0.67
	1st	513.0	264.0	0.67		1st	399.0	272.9	0.70
LA3-SDS	3rd	266.0	81.1	0.21	Riv3-SDS	3rd	209.0	81.3	0.21
	2nd	418.0	81.2	0.21		2nd	342.0	80.7	0.21
	1st	513.0	78.4	0.20		1st	399.0	77.9	0.20

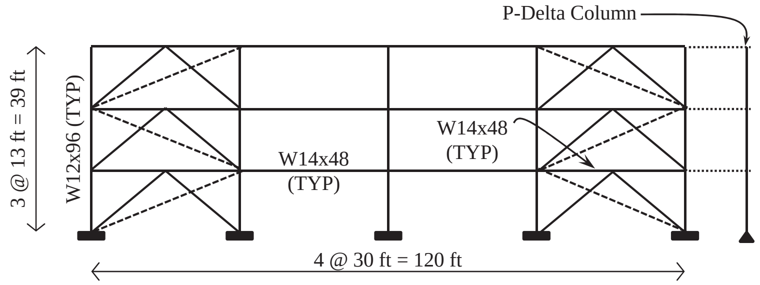

Elevation View

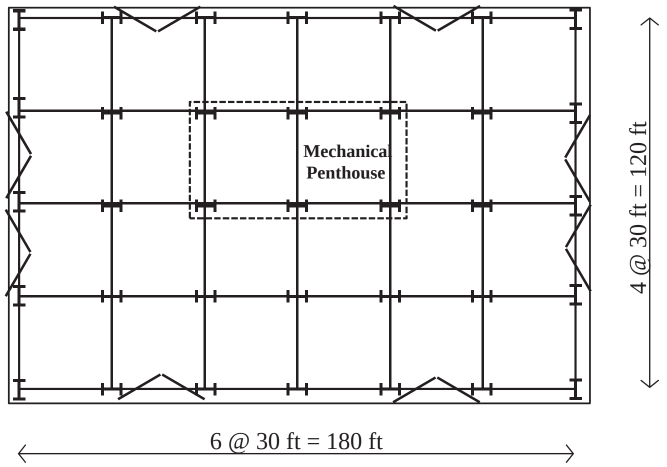

Plan View

Fig. 2. Elevation and plan view of the three-story structure.

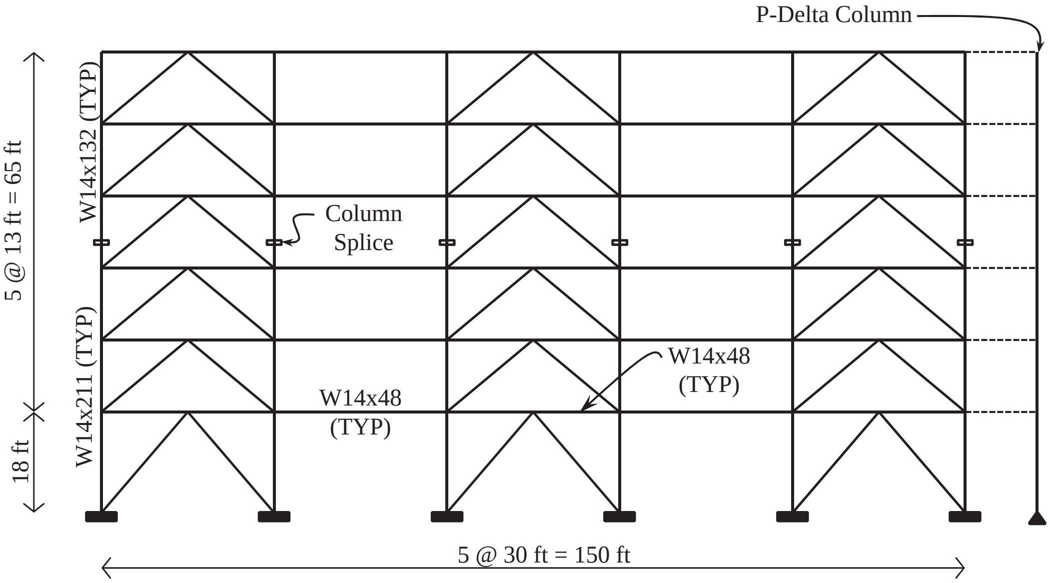

Fig. 3. Elevation view of the six-story structure.

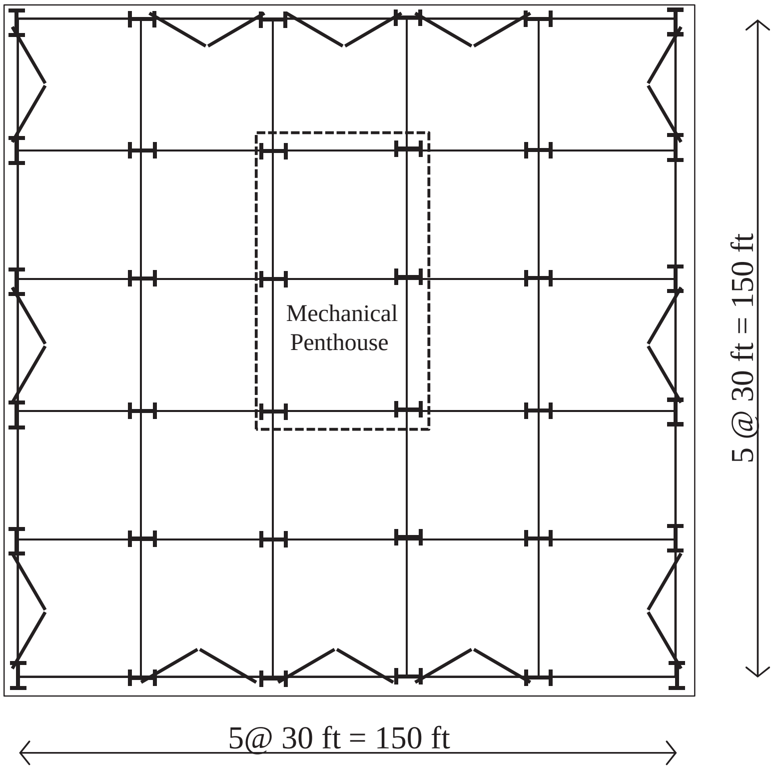

Fig. 4. Plan view of the six-story structure.

Table 3. BRB Properties for Six-Story Building Models

Model	Story Level	Yield Force (kips)	Yield Length (in.)	Yield Length Ratio	Model	Story Level	Yield Force (kips)	Yield Length (in.)	Yield Length Ratio
LA6-CH	6th	57.0	145.9	0.61	Riv6-CH	6th	47.5	145.2	0.61
	5th	76.0	161.7	0.68		5th	66.5	146.3	0.61
	4th	104.5	146.5	0.62		4th	85.5	145.2	0.61
	3rd	114.0	161.4	0.68		3rd	95.0	144.9	0.61
	2nd	123.5	161.4	0.68		2nd	104.5	144.6	0.61
	1st	133.0	199.7	0.71		1st	114.0	197.5	0.70
LA6-CH1.5	6th	76.0	160.5	0.67	Riv6-CH1.5	6th	66.5	146.3	0.61
	5th	104.5	144.6	0.61		5th	95.0	144.9	0.61
	4th	142.5	156.6	0.66		4th	123.5	158.1	0.66
	3rd	161.5	152.9	0.64		3rd	133.0	157.3	0.66
	2nd	180.5	152.2	0.64		2nd	152.0	153.7	0.65
	1st	190.0	190.4	0.68		1st	152.0	192.3	0.68
LA6-CHS	6th	57.0	67.9	0.29	Riv6-CHS	6th	47.5	67.2	0.28
	5th	76.0	66.5	0.28		5th	66.5	68.3	0.29
	4th	104.5	66.6	0.28		4th	85.5	67.2	0.28
	3rd	114.0	66.8	0.28		3rd	95.0	66.9	0.28
	2nd	123.5	66.1	0.28		2nd	104.5	66.6	0.28
	1st	133.0	78.0	0.28		1st	114.0	79.5	0.28
LA6-SD	6th	76.0	292.0	0.74	Riv6-SD	6th	57.0	277.4	0.71
	5th	114.0	290.1	0.74		5th	95.0	276.2	0.70
	4th	152.0	285.0	0.73		4th	123.5	289.3	0.74
	3rd	180.5	283.2	0.72		3rd	133.0	288.6	0.74
	2nd	190.0	282.7	0.72		2nd	152.0	285.0	0.73
	1st	199.5	327.8	0.78		1st	152.0	329.8	0.79
LA6-SDS	6th	76.0	81.2	0.21	Riv6-SDS	6th	57.0	81.1	0.21
	5th	114.0	81.7	0.21		5th	95.0	81.9	0.21
	4th	152.0	81.2	0.21		4th	123.5	81.9	0.21
	3rd	180.5	81.2	0.21		3rd	133.0	81.8	0.21
	2nd	190.0	81.0	0.21		2nd	152.0	81.9	0.21
	1st	199.5	102.6	0.24		1st	152.0	103.5	0.25

at bracing connections. Columns adjacent to braced bays were modeled to account for possible inelasticity. Columns not adjacent to braced bays were modeled elastically. Modal damping of 2% of critical is used for all the modes. Additionally, a small amount of Rayleigh damping is specified (0.05%) over the range of important periods, which is a recommendation of the Perform 3-D manual (CSI, 2011).

Inelastic modeling of the BRB was completed using the BRB compound element. The compound element includes three primary components. The inelastic component uses the length and cross-sectional area of the BRB core to represent yielding and strain hardening with trilinear behavior and a nonsymmetric backbone curve. The nonsymmetric option allows for the different-strength values of the brace in tension and compression. The elastic bar component models the BRB length outside the core (connection region). The third component, the end zone, is the remaining length between the ends of the brace and the beam-column joint working points. The end zone is established as a multiplier on the elastic bar area. The yield force, initial stiffness, post-yield stiffness, and hardening behavior for the inelastic component as well as the length and equivalent area for the elastic bar component and the end-zone multiplier were provided by CoreBrace LLC.

Two different suites of earthquakes were used. The first suite comes from the SAC ground motion suite for LA with a 2% probability of exceedance in 50 years (SAC, 1994). The SAC motions were only used for the LA models. The second suite is a selection of ground motions from FEMA P695 (2009), including motions from the near- and far-field sets. All ground motions are individually scaled such that the average of the suite is at least 90% of the 2% in 50 years hazard spectrum over the range of interest. The ground motion scale factors are shown in Tables 4 (SAC) and 5 (FEMA P695).

RESULTS AND DISCUSSION OF RESULTS

The reported data include story drift, residual story drift, roof acceleration, normalized brace force (or overstrength), cyclic ductility (or single cycle ductility), reference ductility, brace strain, and cumulative ductility. The story drift represents the maximum drift over the height of the structure. The residual drift is the maximum residual story drift over all stories at the end of the analysis. The roof acceleration is the total roof acceleration. The data reported for braces represent the maximum magnitude that occurred in any brace in tension and compression. To ensure that the maximum response in both directions was obtained, data were taken from braces oriented in both directions. The normalized brace force is the maximum force that occurred in any brace in the structure normalized by the brace tension yield force. This approximately represents the overstrength that would be used in a capacity design procedure.

The three different ductility measures all vary in what they represent. Figure 5 shows a representation of the difference between cyclic and reference ductility. The reference ductility demand is measured from the initial, nonelongated core state. This measure is consistent with ductility demands established in specifications such as ANSI/AISC-341 (AISC, 2010a) and is the ductility demand associated with the reported core strain values. The second measure, cyclic (or single-cycle) ductility demand, reports the largest ductility demand from the negative to the positive (or positive to negative) deformation of a single cycle. For symmetrical loading protocols, the cyclic ductility demand would be equal to twice the reference ductility demand. The cumulative inelastic ductility demand represents the summation of the single-cycle excursions throughout the analysis. The force and displacement data from the brace elements was reduced using subroutines that calculated the cyclic and cumulative ductility. The reference ductility was calculated using the maximum brace deformation in tension and compression.

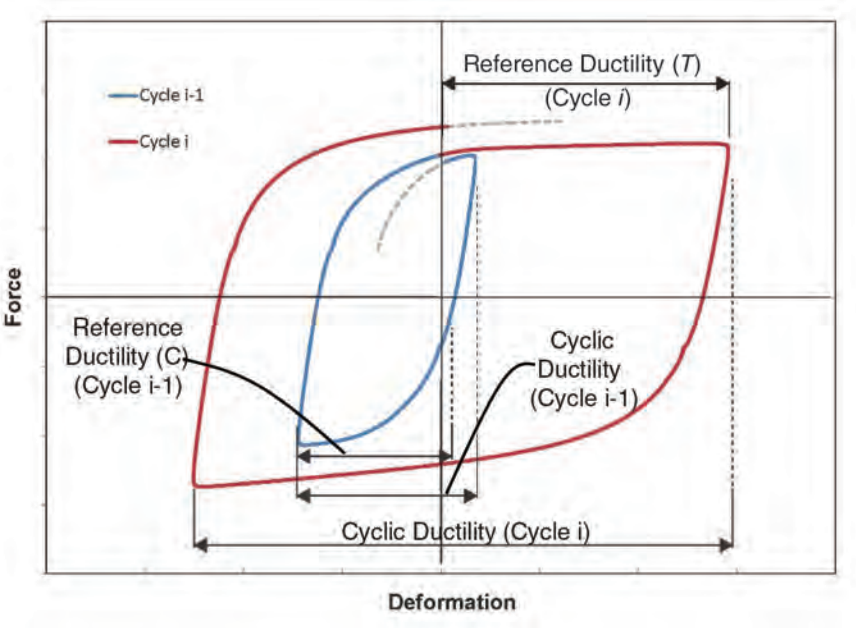

Fig. 5. Schematic representation of ductility demand metrics.

Table 4. SAC Ground Motion Scale Factors

Ground Motion	LA3	LA6	Ground Motion	LA3	LA6
LA21	0.89	0.85	LA31	0.80	0.91
LA22	1.05	1.04	LA32	0.79	0.85
LA23	2.02	2.05	LA33	1.31	1.20
LA24	1.49	0.99	LA34	1.23	1.17
LA25	1.13	1.02	LA35	1.20	1.08
LA26	1.17	0.88	LA36	1.24	0.91
LA27	1.55	1.48	LA37	N/A	1.10
LA28	0.80	0.85	LA38	N/A	0.93
LA29	1.42	1.43	LA39	N/A	1.57
LA30	1.08	1.05	LA40	N/A	1.29

Table 5. FEMA P695 Ground Motion Scale Factors

Ground Motion	LA3	Riv3	LA6	Riv6	Ground Motion	LA3	Riv3	LA6	Riv6
FF01-1	2.13	1.49	1.44	1.04	NF09-1	1.14	0.80	0.51	0.58
FF01-2	1.39	0.98	1.46	1.03	NF09-2	1.96	1.38	1.24	1.13
FF02-1	1.91	1.33	3.45	2.47	NF10-1	1.73	1.22	1.40	1.66
FF02-2	2.06	1.45	2.49	2.13	NF10-2	1.13	0.80	0.82	0.82
FF03-1	1.37	0.96	2.05	1.64	NF12-1	2.13	1.86	1.02	0.75
FF03-2	1.65	1.16	1.73	1.43	NF12-2	2.11	1.47	1.14	0.95
FF09-2	2.65	1.86	3.66	2.69	NF15-1	2.16	1.52	1.65	1.31
FF09-2	2.78	1.97	1.67	1.22	NF15-2	1.60	1.13	2.42	1.97
FF16-1	3.42	2.40	3.02	2.19	NF22-1	1.50	1.06	1.43	1.14
FF16-2	4.20	3.00	3.65	2.45	NF22-2	2.26	1.75	2.17	1.74
FF18-1	2.74	1.92	2.46	1.98	NF23-1	1.50	1.05	1.42	1.20
FF18-2	1.43	1.02	2.13	1.72	NF23-2	1.45	1.02	1.65	1.36
FF19-1	3.30	2.88	2.86	2.46	NF24-1	3.22	2.27	3.30	1.90
FF19-2	2.53	1.79	1.77	1.49	NF24-2	1.52	1.07	1.53	1.28
NF02-1	4.20	2.98	2.09	1.69	NF26-1	2.36	1.66	1.46	1.12
NF02-2	2.55	1.79	1.86	1.42	NF26-2	2.08	1.47	1.80	1.34
NF04-1	1.90	1.66	1.05	0.78	NF27-1	0.92	0.81	0.59	0.53
NF04-2	2.72	1.92	2.37	1.66	NF27-2	2.26	1.59	2.06	1.49
NF06-1	2.50	1.75	2.18	1.70	NF28-1	3.36	2.99	1.85	1.34
NF06-2	2.23	1.67	1.32	0.96	NF28-2	2.47	2.16	1.23	0.92
NF07-1	2.14	1.49	2.93	2.50					
NF07-2	1.50	1.04	1.66	1.23					

FF = far field; NF = near field

Table 6. Analysis Results—Los Angeles Three-Story Structure

Building Model			Story Drift Ratio	Residual Story Drift Ratio	Roof Acceleration (*g*)	Normalized Brace Force	Cyclic Ductility	Reference Ductility	Brace Strain	Cumulative Ductility
P695	LA3-CH	μ	0.036	0.013	1.74	1.92	24.5	23.6	0.031	102.4
		μ+σ	0.051	0.019	2.06	2.21	36.1	34.2	0.045	167.0
	LA3-CH1.5	μ	0.027	0.011	1.86	1.72	18.0	17.9	0.023	67.3
		μ+σ	0.037	0.016	2.25	1.92	26.6	25.3	0.033	102.6
	LA3-CHS	μ	0.026	0.004	1.89	2.40	38.8	32.1	0.042	178.7
		μ+σ	0.035	0.006	2.22	2.84	56.3	44.1	0.058	277.6
	LA3-SD	μ	0.039	0.018	1.60	1.71	15.6	15.4	0.020	64.7
		μ+σ	0.057	0.029	1.89	1.95	22.9	22.7	0.030	103.5
	LA3-SDS	μ	0.025	0.005	2.15	2.34	36.1	29.7	0.039	164.5
		μ+σ	0.034	0.006	2.52	2.75	53.0	41.2	0.054	252.6
SAC	LA3-CH	μ	0.039	0.012	1.90	2.02	29.5	25.7	0.034	110.4
		μ+σ	0.052	0.020	2.12	2.31	46.1	34.8	0.046	147.5
	LA3-CH1.5	μ	0.033	0.013	2.08	1.90	23.8	22.3	0.029	88.0
		μ+σ	0.043	0.019	2.39	2.13	33.4	29.6	0.039	123.2
	LA3-CHS	μ	0.031	0.004	2.11	2.70	47.1	38.5	0.050	204.3
		μ+σ	0.041	0.005	2.37	3.23	68.7	52.5	0.069	265.1
	LA3-SD	μ	0.043	0.019	1.69	1.77	18.4	16.9	0.022	71.9
		μ+σ	0.059	0.031	1.96	2.00	28.6	23.8	0.031	94.6
	LA3-SDS	μ	0.030	0.003	2.25	2.62	43.9	35.1	0.046	194.8
		μ+σ	0.041	0.005	2.50	3.13	64.9	47.9	0.063	258.3
Total	LA3-CH	μ	0.037	0.013	1.78	1.95	25.9	24.2	0.032	104.6
		μ+σ	0.051	0.020	2.09	2.25	39.2	34.4	0.045	163.0
	LA3-CH1.5	μ	0.028	0.011	1.92	1.77	19.6	19.1	0.025	73.1
		μ+σ	0.039	0.017	2.30	1.99	28.9	26.8	0.035	109.5
	LA3-CHS	μ	0.027	0.004	1.95	2.48	41.1	33.9	0.044	185.7
		μ+σ	0.037	0.006	2.28	2.97	60.2	46.8	0.061	276.5
	LA3-SD	μ	0.040	0.018	1.63	1.73	16.4	15.9	0.021	66.7
		μ+σ	0.058	0.030	1.91	1.96	24.7	23.1	0.030	101.9
	LA3-SDS	μ	0.026	0.004	2.18	2.42	38.2	31.2	0.041	172.9
		μ+σ	0.036	0.006	2.53	2.87	56.7	43.3	0.057	256.0

Three-Story Structure

The analysis data are presented in tabular form and include the mean and standard deviation for the suite of earthquakes. Table 6 shows the results from the three-story LA model. The LA data are separated into the SAC and FEMA P695 results. The total results, including both suites combined, are also presented. Table 7 shows the results for the three-story Riverside structure. Table 8 shows the comparison of the results between the various LA and Riverside three-story models. All the results in Table 8 are shown in percentage values. Note that the reference model for the percentage change calculations is indicated in the table. The basis for most of the change calculations is the chevron configuration. However, a supplemental change calculation is provided for the shortened single diagonal as compared to the normal-yield-length single diagonal.

Table 7. Analysis Results—Riverside Three-Story Structure

Building Model		Story Drift Ratio	Residual Story Drift Ratio	Roof Acceleration (*g*)	Normalized Brace Force	Cyclic Ductility	Reference Ductility	Brace Strain	Cumulative Ductility
Riv3-CH	μ	0.030	0.012	1.16	1.80	21.0	19.6	0.026	85.1
	μ+σ	0.044	0.019	1.41	2.14	36.1	33.5	0.044	155.3
Riv3-CH1.5	μ	0.022	0.009	1.31	1.80	14.1	14.1	0.019	52.4
	μ+σ	0.032	0.015	1.57	2.14	21.8	21.2	0.028	91.6
Riv3-CHS	μ	0.022	0.005	1.23	2.22	33.2	28.6	0.037	154.1
	μ+σ	0.034	0.008	1.46	2.70	53.1	44.2	0.058	272.3
Riv3-SD	μ	0.032	0.015	1.12	1.60	12.6	12.3	0.016	51.0
	μ+σ	0.050	0.027	1.33	1.85	20.3	19.3	0.025	90.5
Riv3-SDS	μ	0.022	0.005	1.52	2.15	30.1	25.5	0.033	140.3
	μ+σ	0.031	0.007	1.81	2.58	47.4	37.2	0.049	247.8

Table 8. Analysis Result Comparison—LA and Riverside Three-Story Structures
Percentage Change in Response Quantities (%)

Building Model	Story Drift Ratio	Residual Story Drift Ratio	Roof Acceleration (*g*)	Normalized Brace Force	Cyclic Ductility	Reference Ductility	Brace Strain	Cumulative Ductility
LA 3 Story Structures								
Calculation Basis: Model LA3-CH								
LA3-CH1.5	–22.6	–10.1	7.9	–9.3	–24.2	–21.1	–21.1	–30.2
LA3-CHS	–26.1	–66.9	9.6	27.5	58.8	40.1	40.1	77.6
LA3-SD	9.0	46.5	–8.7	–11.3	–36.8	–34.5	–34.5	–36.2
LA3-SDS	–27.	–64.9	22.4	24.1	47.7	29.0	29.0	65.3
Calculation Basis: Model LA3-SD								
LA3-SDS	–33.9	–76.1	34.0	39.8	133.7	96.8	96.8	159.1
Riverside 3 Story Structures								
Calculation Basis: Model Riv3-CH								
Riv3-CH1.5	–25.6	–23.9	12.7	0.0	–33.0	–27.9	–27.9	–38.4
Riv3-CHS	–24.0	–56.5	5.9	23.8	58.4	45.9	45.9	81.1
Riv3-SD	8.7	25.9	–3.9	–10.9	–39.9	–37.1	–37.1	–40.0
Riv3-SDS	–26.9	–58.6	30.8	19.7	43.3	30.2	30.2	64.9
Calculation Basis: Model Riv3-SD								
Riv3-SDS	–32.7	–67.1	36.1	34.4	138.4	106.9	106.9	174.9

These analysis demands are based on maximum credible earthquake (MCE) level, so comparing them to a code-based check at the design level is not a direct comparison. However, based on a simple multiplier, a 2% drift would be scaled by 1.5 to 3%. While nonlinear response cannot be linearly scaled for an individual analysis, this provides a reasonable basis for comparison. Some general comments on the response are that the Riverside drifts are approximately 3%, while the LA maximum drifts are closer to 4%. The design drift ratios presented in Table 1 are generally well below the allowable drift ratios, but the inelastic response is at or above what might be considered an expected MCE response. The code expectation would be that the values would be the same as both structures LA and Riverside are in Seismic Design Category D. With the exception of the shortened braces at the mean plus one standard deviation, the cumulative ductility demands are within the test parameters for buckling-restrained braces in the AISC *Seismic Provisions* (2010a).

The three-story model results indicate several things based on the differences between the two standard brace configurations, chevron and single diagonal. For the typical brace configurations (CH and SD), the single diagonal is more flexible and experiences greater story and residual drifts. The increase in story drifts for the single diagonal compared to the chevron was 9.0 and 8.7% for LA and Riverside, respectively. The increase in residual drift for single diagonal over chevron braces was 46.5 and 25.9% for LA and Riverside, respectively. The trade-off is that the normalized brace force, reference ductility, and cumulative inelastic ductility are lower for the single diagonal. The decrease in normalized brace force in the single diagonal compared to the chevron is approximately 11%. The decrease in the reference ductility demand of single diagonals is 34.5% for LA and 37.1% for Riverside. The decrease in cumulative ductility is 36.2 and 40.0%, respectively, for LA and Riverside. The differences are due to the longer brace yielding length and the longer fundamental period of the single-diagonal structure. The chevron configuration designed with $I_e = 1.5$ results in improved performance in all aspects with the exception of the roof acceleration when compared to the normal risk category design. This increased acceleration is based on the decreased period of vibration.

The shortened brace length (CHS and SDS), which represents an extreme value and may be impractical, has a significant impact on performance. This shortened brace length and the 50% strength increase ($I_e = 1.5$) have a similar impact on the fundamental period of vibration. The reduction in maximum story drifts for the shortened braces ranges from 24 to 34%. The reduction in residual drifts ranges from 57 to 76% for the various three-story models. All other performance metrics result in larger component and system demands when using the shortened yield length. Some metrics change radically. The largest increase is shown in the ductility metrics. The cumulative ductility demand increase for the shortened braces ranges between a 78% increase for the LA chevron up to a 175% increase for the Riverside single diagonal. It should be noted that the relative change in yield length is greater for the single-diagonal configurations, which may be one reason for the larger changes in demands. The reference ductility demand for shortened braces is increased by 46 and 107% for the Riverside chevron and single diagonal, respectively. The increases in reference ductility for LA chevron and single-diagonal shortened braces are 40 and 97%, respectively. The increases in normalized brace force range between 28% for the LA chevron and 40% for the LA single diagonal. Even though the shortened braces experience significantly higher demands, the mean value for cumulative ductility is less than the cumulative demand of 200 from the AISC *Seismic Provisions* qualification protocol. However, the brace demands at mean plus one standard deviation do exceed the qualification test requirement.

Table 9 shows a comparison between the Riverside and the LA three-story response with LA as the basis for the calculation of percentage change. Because the SAC records were not run on the Riverside structure, the most direct comparison of seismic hazard is the FEMA P695 records. The only difference in this case is the scale factor, which is based on the hazard. The biggest difference when looking at the two hazards is the roof acceleration. In all cases, as one would expect, the roof acceleration of the Riverside structures has been reduced to approximately 70% of the value for LA. The other metrics also generally decrease with a few exceptions. It is noteworthy that the metric that had the least impact from the decrease in ground acceleration is the residual drift.

One additional discussion point is the difference between the SAC and FEMA P695 records. The SAC records produce an increased response (higher demands) for everything except the residual drift results. The records for both suites were scaled using the same method to ensure that the mean of the scaled suite did not fall below 90% of the MCE spectrum over the important period range. There is variability in general with ground motion records; however, the SAC records do have a generally higher mean for most of the response quantities reported. As an example, the story drifts under the SAC records increased between 10 and 21%, depending on the structure. The cyclic ductility demand increased from 19 to 32%, and the reference ductility demands increased from 9 to 25%. All these are indicators that this suite of earthquakes is severe and many have large pulses, which have increased certain types of response.

Figure 6 plots brace strain versus normalized brace force for six of the three-story structures. In these plots, the maximum tension and compression value in a first-floor brace are plotted for each record. This provides a better view of

Table 9. Analysis Result Comparison—LA and Riverside Three-Story Structures Percentage Change in Response Quantities (%)

Building Model	Story Drift Ratio	Residual Story Drift Ratio	Roof Acceleration (*g*)	Normalized Brace Force	Cyclic Ductility	Reference Ductility	Brace Strain	Cumulative Ductility
Calculation Basis: Equivalent LA Model (i.e., Riv3CH/LA3-CH)								
Riv3-CH	–17.3	–5.4	–33.1	–6.3	–14.3	–16.9	–16.9	–16.9
Riv3-CH1.5	–18.2	–14.9	–29.7	4.8	–22.0	–20.9	–20.9	–22.2
Riv3-CHS	–13.2	17.8	–35.0	–7.3	–14.4	–10.9	–10.9	–13.7
Riv3-SD	–17.7	–16.7	–30.3	–6.6	–19.0	–20.1	–20.1	–21.2

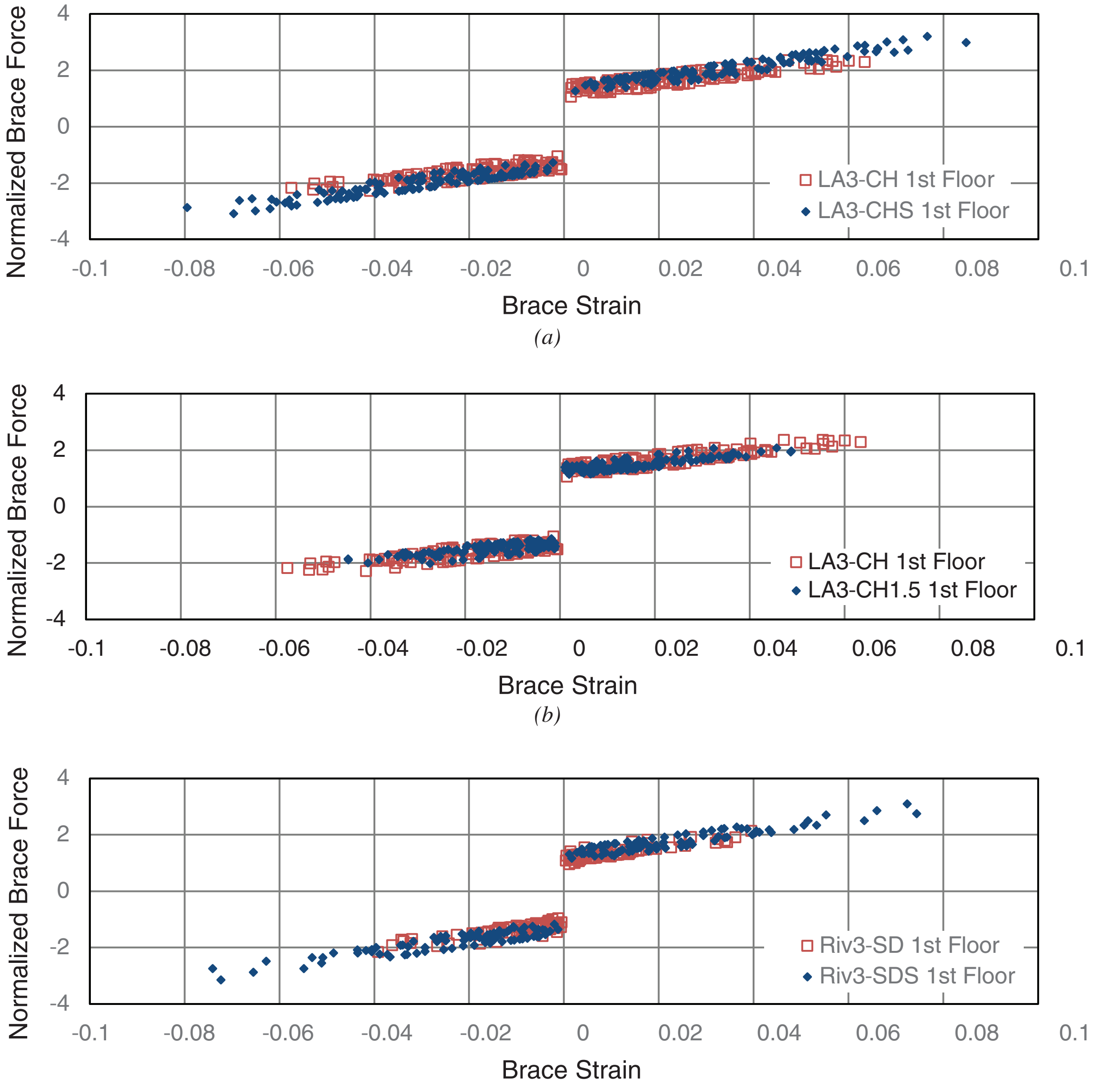

(a)

(b)

(c)

Fig. 6. Brace strain vs. normalized brace force for three-story structures: (a) LA chevron; (b) LA chevron; (c) Riverside single diagonal.

how the data are distributed for the various ground motion records. Figure 6(a) shows the benefits of the importance factor. It is clear that the brace strain is reduced by designing the brace for the higher force demands associated with the higher importance factor. From the Figure 6(b) and 6(c) plots, it can be seen that the shortened-yield-length brace produces a substantial increase in maximum brace force and maximum brace strain. It can also be seen that the single diagonal experiences greater demand increases than the chevron configuration. It should be noted again that these yield lengths are very short, resulting in large normalized brace forces and strains. Some of these strains may be unrealistic in common BRB designs without fracturing the core.

Six-Story Structure

Table 10 shows the analysis results for the LA six-story structures. Table 11 shows the results for the Riverside six-story structures. Table 12 shows the relative percentage change in response quantities for the six-story models using a consistent methodology as was presented previously for the three-story models.

Many similar trends are seen in the six-story results. Just as with the three-story model, a seismic importance factor of 1.5 decreased the story drift by 14% for LA and 18% for Riverside while also decreasing all the ductility metrics by at least 9%. The cumulative ductility demand was decreased by 12 and 9.8% for LA and Riverside, respectively. The shortened-yield-length braces decreased both the story drift and the residual story drift, but in both cases, they increased the ductility measures by at least 107% and by as much as 200%. Again, some of these brace demands are likely not achievable. The normalized force (overstrength) in shortened braces increased by 18% for the chevron and 51% for the single diagonal compared to the equivalent standard-yield-length braces. The percentage increases in demands were greater for the single diagonal as the relative shortening of the single diagonal was much greater.

Table 13 shows a comparison between the Riverside and the LA six-story response with LA as the basis for the calculation of percentage change. As with the three-story, only the P695 ground motions are included in the comparison. The biggest difference when looking at the two hazards is the roof acceleration. In all cases, as one would expect, the roof acceleration of the Riverside structures has been reduced to approximately 77% of the value for LA. This is a smaller reduction in roof acceleration than was seen in the three-story structures. The other metrics also generally decrease, with a few exceptions. One exception is the residual drift. While all the other models showed a decrease of residual drift in Riverside, the chevron had a significant increase (83%) in residual drift, which is unusual. The data for the Riverside residual drift show two of the near-field motions resulting in approximately 5% residual drift and three other near-field records showing greater than 3% residual drift. Utilizing near-field motions for a hazard such as Riverside may be questionable, and the accuracy of residual drifts is also questionable. Due to the lower strength, the Riverside structure was less able to absorb the large energy of a near field record resulting in large drifts and residual drifts.

Figure 7 shows plots of the maximum brace strain and normalized brace force for a selection of the six-story models. The plots in Figures 7(a) and 7(b) show that for both the chevron and single-diagonal configuration, the demands in the upper-story braces are not as large as for the first story, but there is significant inelastic behavior over the height of the structure. For the chevron, the fourth-story brace still experiences greater than 4% strain in several of the quake records, while the first-story brace has several values exceeding 6%. The single diagonal has lower strain levels due to the longer yield length, but the fourth-floor braces experience strains in excess of 2%.

The plot in Figure 7(c) shows the difference between the Risk Category II and IV chevron structures. The differences for the six-story frame are not as significant as for the three-story structure. This is visible in the plot and also shown by the data. Figure 7(d), which has a different scale from the other plots, shows that the effect of the shortened brace is significant for the six-story structure and extends up the building height. Brace strains in excess of 5%, which may not be feasible, result even in the upper floors of the structure.

Table 14 shows a comparison of results for both locations between the different structure heights. The basis of the calculations is the three-story model response. The six-story structures, on average, experienced an increase in maximum story drift over the three-story counterparts. For the LA buildings, the increase ranged from 1.0% for the single diagonal up to 33% for the short-yield-length chevron. The Riverside structure exhibited a 6.3% decrease for the single-diagonal maximum story drift, while all the other configurations increased for the six-story structure by between 9 and 24%. The residual drifts were a more mixed comparison. For LA, the six-story structures had lower residual drifts than the three-story structures for all cases with the exception of the shortened chevron. The residual drift for the six-story shortened-yield chevron structure was nearly double the three-story version. For the six-story Riverside structures, all the residuals decreased from the three-story results with the exception of the chevron, which increased by 45%. The roof accelerations decreased for the six-story buildings for all cases by at least 30% when compared to the three-story buildings. This is expected due to the longer period of vibration.

The metrics representing brace demands also changed from the three- to the six-story buildings. For LA, the normalized brace force increased for all cases of the

Table 10. Analysis Results—Los Angeles Six-Story Structure

Building Model			Story Drift Ratio	Residual Story Drift Ratio	Roof Acceleration (*g*)	Normalized Brace Force	Cyclic Ductility	Reference Ductility	Brace Strain	Cumulative Ductility
P695	LA6-CH	μ	0.036	0.009	0.85	1.90	23.0	19.5	0.026	102.4
		μ+σ	0.051	0.016	1.10	2.20	35.5	28.0	0.037	167.0
	LA6-CH1.5	μ	0.031	0.010	0.95	1.82	20.6	17.4	0.023	89.7
		μ+σ	0.043	0.016	1.26	2.06	29.6	24.3	0.032	140.6
	LA6-CHS	μ	0.033	0.008	0.91	2.25	57.5	43.6	0.057	269.3
		μ+σ	0.046	0.013	1.21	2.60	87.3	62.9	0.082	425.4
	LA6-SD	μ	0.035	0.011	0.98	1.74	17.3	14.9	0.020	82.0
		μ+σ	0.051	0.020	1.27	1.99	26.8	21.8	0.029	129.4
	LA6-SDS	μ	0.029	0.004	1.17	2.63	47.4	36.6	0.048	247.5
		μ+σ	0.042	0.007	1.49	3.23	68.8	53.6	0.070	380.7
SAC	LA6-CH	μ	0.048	0.012	0.89	2.14	31.7	26.4	0.035	108.1
		μ+σ	0.068	0.019	1.01	2.45	43.0	36.8	0.048	137.4
	LA6-CH1.5	μ	0.042	0.012	1.06	2.05	29.8	24.3	0.032	96.6
		μ+σ	0.058	0.019	1.25	2.34	41.9	33.3	0.044	121.9
	LA6-CHS	μ	0.044	0.009	0.95	2.50	78.7	58.7	0.077	275.8
		μ+σ	0.060	0.012	1.09	2.88	106.3	81.0	0.106	348.0
	LA6-SD	μ	0.051	0.016	1.03	1.95	24.2	21.4	0.028	82.6
		μ+σ	0.071	0.027	1.16	2.21	33.4	30.0	0.039	103.7
	LA6-SDS	μ	0.042	0.004	1.27	3.20	64.4	52.4	0.069	254.2
		μ+σ	0.062	0.006	1.47	4.01	85.9	77.0	0.101	311.3
Total	LA6-CH	μ	0.040	0.010	0.87	1.98	25.8	21.7	0.028	108.2
		μ+σ	0.058	0.017	1.08	2.30	38.6	31.5	0.041	162.0
	LA6-CH1.5	μ	0.034	0.011	0.99	1.90	23.5	19.6	0.026	91.9
		μ+σ	0.049	0.017	1.27	2.17	34.5	27.9	0.037	136.3
	LA6-CHS	μ	0.036	0.008	0.93	2.33	64.4	48.5	0.064	271.4
		μ+σ	0.052	0.012	1.18	2.71	95.1	70.0	0.092	406.3
	LA6-SD	μ	0.040	0.013	1.00	1.81	19.5	17.0	0.022	82.2
		μ+σ	0.059	0.023	1.25	2.08	29.5	25.1	0.033	123.0
	LA6-SDS	μ	0.034	0.004	1.20	2.81	52.9	41.7	0.055	249.6
		μ+σ	0.050	0.006	1.49	3.54	75.7	62.8	0.082	364.0

Table 11. Analysis Results—Riverside Six-Story Structure

Building Model		Story Drift Ratio	Residual Story Drift Ratio	Roof Acceler-ation (*g*)	Normalized Brace Force	Cyclic Ductility	Reference Ductility	Brace Strain	Cumulative Ductility
Riv6-CH	μ	0.033	0.017	0.640	1.81	19.3	18.0	0.024	84.9
	μ+σ	0.048	0.031	0.824	2.10	29.5	26.5	0.035	136.8
Riv6-CH1.5	μ	0.027	0.008	0.729	1.81	17.5	15.2	0.020	76.6
	μ+σ	0.037	0.014	0.959	2.10	25.2	20.8	0.027	119.6
Riv6-CHS	μ	0.025	0.005	0.738	2.41	39.8	32.1	0.042	185.7
	μ+σ	0.035	0.007	0.974	2.90	58.2	46.2	0.060	290.1
Riv6-SD	μ	0.030	0.010	0.757	1.63	14.1	12.6	0.017	69.9
	μ+σ	0.044	0.019	1.004	1.86	22.0	18.5	0.024	113.4
Riv6-SDS	μ	0.026	0.003	0.886	2.29	42.7	32.8	0.043	220.0
	μ+σ	0.039	0.005	1.148	2.87	62.7	48.4	0.063	337.1

Table 12. Analysis Result Comparison—LA and Riverside Six-Story Structures
Percentage Change in Response Quantities (%)

Building Model	Story Drift Ratio	Residual Story Drift Ratio	Roof Acceler-ation (*g*)	Normalized Brace Force	Cyclic Ductility	Reference Ductility	Brace Strain	Cumulative Ductility
LA Six-Story Structures								
Calculation Basis: Model LA6-CH								
LA6-CH1.5	–14.3	7.9	11.5	–4.2	–10.5	–10.5	–10.5	–12.4
LA6-CHS	–9.3	–13.9	6.8	18.0	150.1	124.3	124.3	163.0
LA6-SD	–1.3	21.4	14.6	–8.6	–25.0	–23.3	–23.3	–19.9
LA6-SDS	–17.8	–58.2	37.2	38.4	106.2	88.2	88.2	141.7
Calculation Basis: Model LA6-SD								
LA6-SDS	–16.7	–65.6	19.7	51.4	174.9	145.3	145.3	201.8
Riverside Six-Story Structures								
Calculation Basis: Model Riv6-CH								
Riv6-CH1.5	–17.8	–51.8	13.9	0.0	–9.0	–15.7	–15.7	–9.8
Riv6-CHS	–26.0	–73.6	15.3	33.2	106.8	78.2	78.2	118.7
Riv6-SD	–9.3	–41.3	18.2	–9.7	–26.8	–30.1	–30.1	–17.7
Riv6-SDS	–20.1	–83.5	38.4	26.6	121.4	81.6	81.6	159.0
Calculation Basis: Model Riv6-SD								
Riv6-SDS	–11.9	–71.8	17.1	40.3	202.2	159.7	159.7	214.9

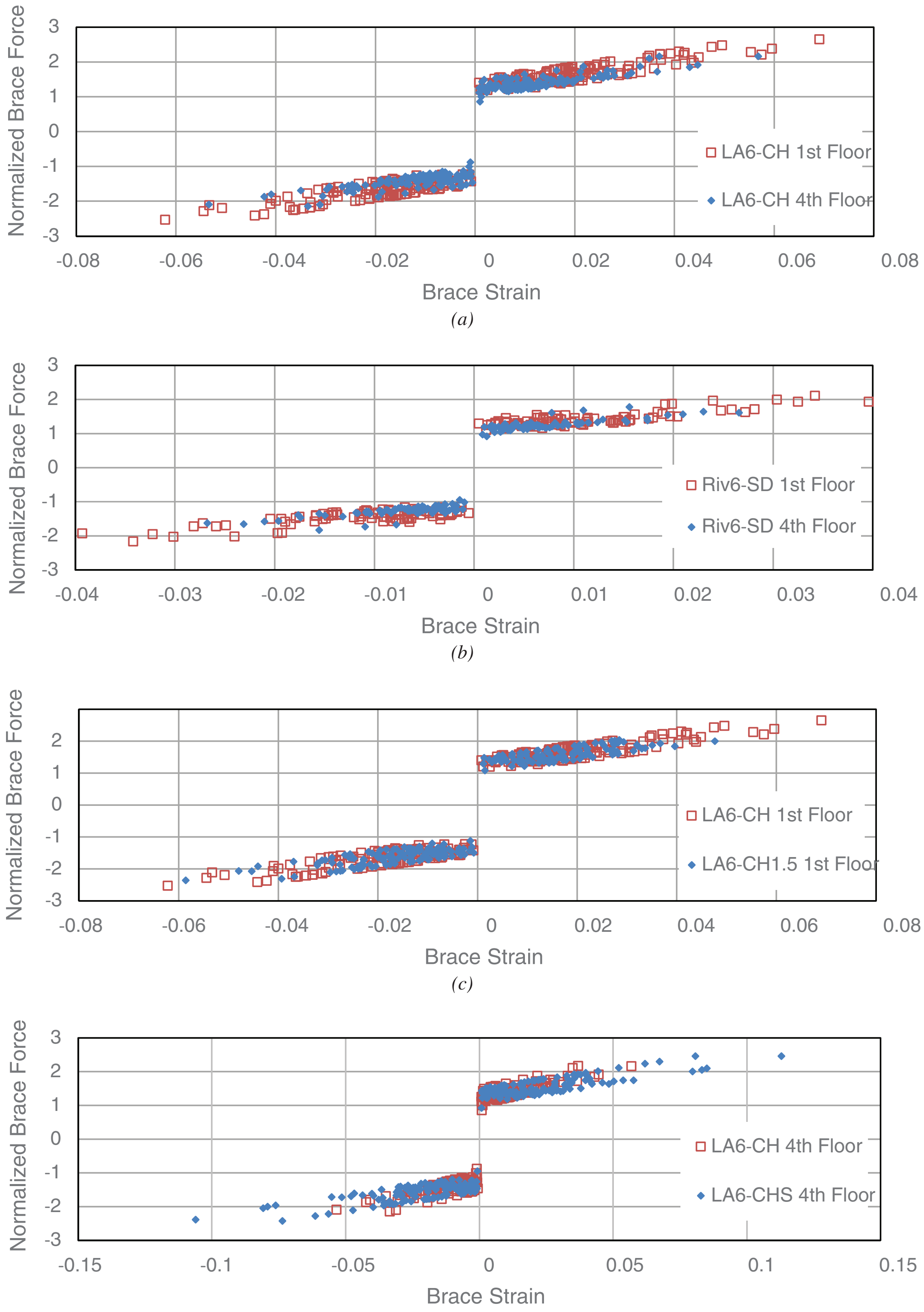

(a)

(b)

(c)

(d)

Fig. 7. Brace strain vs. normalized brace force for six-story structures: (a) LA chevron; (b) Riverside single diagonal; (c) LA chevron and I = *1.5 chevron; (d) LA chevron and shortened chevron.*

Table 13. Analysis Result Comparison—LA and Riverside Six-Story Structures
Percentage Change in Response Quantities (%)

Building Model	Story Drift Ratio	Residual Story Drift Ratio	Roof Acceler-ation (*g*)	Normal-ized Brace Force	Cyclic Ductility	Reference Ductility	Brace Strain	Cumulative Ductility
Calculation Basis: Equivalent LA Model (i.e., Riv6CH/LA6-CH)								
Riv6-CH	–7.6	82.8	–25.0	–4.8	–16.2	–7.3	–7.3	–17.1
Riv6-CH1.5	–11.3	–18.3	–23.4	–0.7	–14.8	–12.7	–12.7	–14.6
Riv6-CHS	–24.6	–43.9	–19.1	7.4	–30.7	–26.4	–26.4	–31.1
Riv6-SD	–15.1	–11.6	–22.7	–6.0	–18.2	–15.5	–15.5	–14.8
Riv6-SDS	–10.2	–27.6	–24.4	–12.9	–10.1	–10.6	–10.6	–11.1

Table 14. Analysis Result Comparison —LA and Riverside Six-Story to Three-Story Structures
Percentage Change in Response Quantities (%)

Building Model	Story Drift Ratio	Residual Story Drift Ratio	Roof Acceler-ation (*g*)	Normal-ized Brace Force	Cyclic Ductility	Reference Ductility	Brace Strain	Cumulative Ductility
LA Structures								
Basis of Calculation: Equivalent LA3 Model (i.e., LA6-CH/LA3-CH)								
LA6-CH	8.8	–17.7	–51.3	1.6	–0.3	–10.3	–10.3	3.4
LA6-CH1.5	21.4	–5.0	–48.6	7.4	20.0	2.9	2.9	25.8
LA6-CHS	33.0	99.4	–52.6	–6.3	56.7	43.2	43.2	46.1
LA6-SD	1.0	–28.9	–38.8	4.5	19.2	7.3	7.3	23.2
LA6-SDS	27.1	–9.1	–44.7	16.5	38.4	33.7	33.7	44.4
Riverside Structures								
Basis of Calculation: Equivalent Riv3 Model (i.e., Riv6-CH/Riv3-CH)								
Riv6-CH	12.3	44.5	–44.9	0.7	–8.1	–8.0	–8.0	–0.2
Riv6-CH1.5	24.1	–8.4	–44.3	0.7	24.7	7.6	7.6	46.2
Riv6-CHS	9.3	–12.2	–40.0	8.4	20.0	12.3	12.3	20.5
Riv6-SD	–6.3	–32.6	–32.2	2.0	11.9	2.3	2.3	36.9
Riv6-SDS	22.7	–42.2	–41.7	6.5	41.9	28.3	28.3	56.8

six-story structure except the shortened yield chevron, which decreased by 6%. The increases ranged from 2 to 16%. An increase in the normalized brace force occurred for all the Riverside six-story configurations. These increases ranged from 1 to 8%. The ductility metrics also generally increased from the three- to the six-story response. The most substantial increases were seen in the shortened yield length configurations. The LA chevron configuration showed the same single-cycle ductility demand and a 10% decrease for the six-story frame in the reference ductility demand and brace strain. The chevron configuration in Riverside showed an 8% decrease from the three- to the six-story building for the single-cycle ductility, reference ductility, and brace strain. The cumulative inelastic ductility demand for the six-story chevron increased by 3% for LA and remained constant for Riverside. The chevron with a 1.5 importance factor and the single diagonal experienced similar trends. Double-digit percentage increases (12 to 46%) for the six-story frame compared to the three-story were seen for the normalized brace force and the cumulative inelastic ductility demand for both LA and Riverside. The reference ductility demand and brace strain increased from 2 to 8% for both brace configurations in both locations. The ductility metrics for the shortened yield length braces all increased by at least 20% for the six-story design. The maximum increases were over 50%, which occurred in the single-cycle ductility demand for the shortened chevron in LA and the cumulative inelastic ductility demand for the Riverside shortened single diagonal.

In general, the performance trends for the different structures behaved as would be expected. The prime example of the deviation was with the residual drifts. The general trends that should be highlighted include the beneficial effect of the importance factor. With the exception of the expected increase in acceleration due to the stiffening effect, all performance metrics were reduced. The effect of the seismic hazard was also interesting as the increase in hazard produced a larger drift demand on the structure. The basis of the code is to maintain the same standard for all structures in a similar Seismic Design Category. The same drift limits and seismic performance factors apply consistently to both structures, but the higher spectral accelerations produced larger demands. Some of this could be attributed to the LA structures having greater stiffness (lower period), which would further increase the accelerations more than just the change spectral accelerations. The shortened-yield-length braces demonstrated the benefit of stiffness in reducing drifts; however, the high cost of maximum brace forces and potentially unobtainable brace strains were particularly troubling.

Cyclic to Reference Ductility Ratio

One other notable aspect is the ratio between cyclic and reference ductility. This is of particular interest because the qualification testing required for BRB in the AISC *Seismic Provisions* (2010a) is based on an increasing-amplitude, symmetric cyclic protocol. This protocol induces a 2:1 ratio between the cyclic and the reference ductility as part of the qualification. The ratios from each record for the LA6-CH are shown in Table 15. In this table, the ratios are broken out by the different subgroups of the ground motion suite. For each of the ground motions, the maximum single-cycle ductility and the reference ductility are shown as well as the ratio of the single cycle to the reference ductility. The average of the three individual subgroups and the overall ground motion suite are shown. The overall average is 1.2. The P695 far-field group has the highest mean of 1.3, while the P695 near-field subgroup has the lowest average at 1.1. This indicates that the far-field events are generally more symmetric than near-field events and result in larger ratios, which are still significantly less than 2. It is interesting to note that in some cases, the ratio is less than 1.0, which indicates that it took multiple smaller cycles to get to the maximum reference inelastic excursion. This is what is sometimes called the ratcheting effect. This indicates that the symmetric loading protocol with a ratio of 2 may not be the best representation of what occurs in a real earthquake event. It also indicates that the maximum inelastic forces, which are based on tests from the symmetric protocol, may not be representative of what occurs in an actual seismic event. Reference strain limits established from symmetric loading protocols are also conservative because they are produced from cyclic strains that are double in value the reference strain. In actual earthquake events, the reference strains will more likely be based on cyclic strains of the same or a similar amplitude. This research indicates that it may be more representative to generate a different testing protocol that is more representative of actual performance. An example of a nonsymmetric, near-fault protocol was recently developed for a BRB in a long-span bridge (Lanning et al., 2016).

BRB Elastic Stiffness Variation

Unlike other structural steel lateral-resisting systems, BRB are generally analyzed to a higher degree to determine the elastic stiffness used in a model. This is done to account for the significant changes in axial rigidity of BRB due to the different cross-sectional properties along the brace length. At some level, this must be done, but a reasonable, simple approximation is likely sufficient. The challenge is that until the design is complete and a BRB manufacturer has provided the geometry, detailed information may not be available, and thus a method for making reasonable approximations is desirable. For concentrically braced frames, the effect of the brace being shortened, the gusset plate, and the beam-column joint are not included in determining the actual brace stiffness, nor is this required by design standards. For reduced beam section (RBS) moment frame connections, the only requirement is that elastic displacements in the model are increased by 10% for flange reductions of up to 50% of the flange width (AISC, 2010b).

In order to investigate the impact of the elastic stiffness on structural response, some of the previous models were run with the elastic stiffness modified by 10% of the value provided by CoreBrace. The models included both a 10% increase and decrease in the stiffness values. The strength values and post-yield behavior remained as they were in the previous analyses. The results of these analyses are presented in Table 16. The entries for the LA6-CH90 indicates the six-story chevron brace with 90% of the CoreBrace provided stiffness, while LA6-CH110 uses 110% of the provided stiffness. The same is true for the single diagonal brace shown. The six-story models of the LA chevron and single diagonal both showed that a 10% change in initial stiffness resulted in maximum changes in response up to 2.7% (residual drift). When looking at the brace demands and the story drift, the maximum change was about 1.3%, indicating that from the perspective of a nonlinear dynamic analysis, the exact

Table 15. Cyclic and Reference Ductility Results—LA Six-Story Chevron

Earthquake Record	Cyclic Ductility	Reference Ductility	Cyclic to Reference Ductility Ratio	Earthquake Record	Cyclic Ductility	Reference Ductility	Cyclic to Reference Ductility Ratio
FF01-1	11.6	14.3	0.8	NF02-1	19.3	17.4	1.1
FF01-2	16.3	11.5	1.4	NF02-2	53.2	45.5	1.2
FF02-1	29.5	25.4	1.2	NF04-1	27.3	18.0	1.5
FF02-2	10.2	9.4	1.1	NF04-2	20.7	20.9	1.0
FF03-1	16.7	16.5	1.0	NF06-1	28.8	19.7	1.5
FF03-2	15.6	12.9	1.2	NF06-2	26.6	27.4	1.0
FF09-1	59.3	36.2	1.6	NF07-1	20.3	20.2	1.0
FF09-2	16.4	16.4	1.0	NF07-2	29.2	33.5	0.9
FF16-1	25.3	23.5	1.1	NF09-1	9.2	9.2	1.0
FF16-2	32.9	23.6	1.4	NF09-2	15.9	11.9	1.3
FF18-1	13.8	9.6	1.4	NF10-1	18.8	16.5	1.1
FF18-2	8.5	6.7	1.3	NF10-2	14.2	13.1	1.1
FF19-1	59.4	37.8	1.6	NF12-1	27.1	18.2	1.5
FF19-2	52.8	31.9	1.7	NF12-2	20.5	16.8	1.2
P695 far-field mean			1.3	NF15-1	10.7	14.0	0.8
P695 far-field mean + standard deviation			1.5	NF15-2	34.9	28.5	1.2
LA21	21.5	15.2	1.4	NF22-1	21.6	23.3	0.9
LA22	21.4	23.4	0.9	NF22-2	18.9	14.0	1.4
LA23	33.9	20.7	1.6	NF23-1	13.0	14.4	0.9
LA24	38.1	34.2	1.1	NF23-2	13.3	10.8	1.2
LA25	23.7	25.4	0.9	NF24-1	14.7	18.3	0.8
LA26	19.9	14.9	1.3	NF24-2	16.6	14.5	1.1
LA27	41.0	32.1	1.3	NF26-1	31.4	33.2	0.9
LA28	21.3	22.1	1.0	NF26-2	16.1	17.5	0.9
LA29	14.7	12.4	1.2	NF27-1	15.5	11.8	1.3
LA30	32.4	26.4	1.2	NF27-2	14.6	19.6	0.7
LA31	19.2	17.4	1.1	NF28-1	22.3	15.0	1.5
LA32	17.9	11.7	1.5	NF28-2	29.2	18.7	1.6
LA33	34.6	24.1	1.4	P695 near-field mean			1.1
LA34	31.5	22.4	1.4	P695 near-field mean + standard deviation			1.4
LA35	54.9	52.7	1.0	Ground motion suite mean			1.2
LA36	49.5	42.2	1.2	Ground motion suite mean + standard deviation			1.4
LA37	38.3	26.7	1.4				
LA38	42.4	28.8	1.5				
LA39	30.5	30.8	1.0				
LA40	50.1	43.9	1.1				
SAC mean			1.2				
SAC mean + standard deviation			1.5				

Table 16. Analysis Results with Initial Stiffness Variation—Los Angeles Six-Story Structure

Building Model		Story Drift Ratio	Residual Story Drift Ratio	Roof Acceleration (*g*)	Normalized Brace Force	Single Cycle Ductility	Reference Ductility	Brace Strain	Cumulative Ductility
LA6-CH	μ	0.040	0.010	0.87	1.98	25.8	21.7	0.028	108.2
LA6-CH90	μ	0.040	0.011	0.86	1.99	25.7	21.9	0.029	106.6
Percent change		0.65	1.70	–1.09	0.34	–0.56	0.78	0.53	–1.50
LA6-CH110	μ	0.039	0.010	0.88	1.97	25.8	21.4	0.028	108.6
Percent change		–1.05	–2.72	1.76	–0.34	0.11	–1.23	–1.31	0.38
LA6-SD	μ	0.040	0.013	1.00	1.81	19.5	17.0	0.022	82.2
LA6-SD90	μ	0.041	0.013	0.98	1.81	19.4	17.2	0.023	82.2
Percent change		1.28	0.20	–1.71	0.19	–0.69	0.89	0.81	0.03
LA6-SD110	μ	0.040	0.013	1.02	1.80	19.6	16.8	0.022	82.2
Percent change		–1.20	–0.56	2.50	–0.25	0.43	–0.98	–1.22	0.05

stiffness value is not something for which the analysis or the actual response would be highly sensitive. It is important to have a simple approach for engineers to determine a reasonable value for the stiffness of a BRB in an elastic design model without needing a detailed geometry of the brace during the design phase. This is further highlighted by the fact the while the LA3-SD had a design drift of 1.86 times that of LA3-CH, the difference in the nonlinear drift of LA3-SD was only 9% greater than for LA3-CH. Similar trends apply to the other models as well. This is an additional indicator of the fact that while the elastic drifts are important, with all the other assumptions inherent in analyzing structures, a detailed assessment of the BRB stiffness is not required.

SUMMARY AND CONCLUSION

This paper reports on an analytical study on structures with buckling restrained braces using two different seismic hazards and two structure heights coupled with single-diagonal and chevron brace configurations. Several additional parameters were also included to investigate the system performance, brace force, and ductility demands of BRB frames. The 2D nonlinear dynamic analyses were completed with a large suite of earthquakes that included both near-field and far-field records. The important findings and conclusions include:

- The performance of the BRB is within the expected bounds of the code-based limits using the seismic performance factors.
- Many parameters have an influence on the ductility and force demands in BRB, including the brace configuration, importance factor, seismic hazard, and brace yield length. In general, these changes in response follow the expected trends with the primary exception being residual drifts.
- The importance factor has a beneficial effect on brace forces, ductility demands, and story drift. In most cases, it reduces residual drifts, but results in increased roof accelerations as would be expected due to the dynamic properties of the structures.
- The shortened-yield-length braces experienced smaller story and residual story drifts. However, this is coupled with significant increases in acceleration, normalized force demands, and all measures of brace ductility demand. Limits on the yield length of BRB should be considered to avoid the potential for high strains, large forces, or other undesirable effects. Designing to a higher strength may be a better solution if stiffness of the braces needs to be improved. This would result in lower demands in all aspects of the response with the exception of the expected acceleration increase, which would increase with any stiffening of the structure.
- Brace inelastic response was distributed to all levels of the structure with little indication of the potential for developing a soft story due to a single level of braces experiencing all the inelastic response.
- The ratio of the cyclic to reference ductility demand is generally much lower than what results from the symmetric testing protocols for BRB in the AISC *Specification*. This indicates that the forces due to analytical hardening rules determined from testing results may not be consistent with the hardening that occurs due to an actual earthquake. This could have

a potential impact on the expected strength values used as the capacity design elements in BRB system designs.

- The impact of the brace elastic stiffness on the nonlinear response of the models was minimal. The nonlinear analysis demonstrated that structures with significantly different design drift ratios did not have nearly the same difference in inelastic drift ratios. This indicates that assumed brace stiffness values used in design that are sufficiently accurate for elastic models.

REFERENCES

AISC (2010a), *Seismic Provisions for Structural Steel Buildings*, ANSI/AISC-341, American Institute of Steel Construction, Chicago, IL.

AISC (2010b), *Prequalified Connections for Special and Intermediate Steel Moment Frames for Seismic Applications*, American Institute of Steel Construction, Chicago, IL.

ASCE (2010), *Minimum Design Loads for Buildings and Other Structures*, ASCE/SEI 7, American Society of Civil Engineers, Reston, VA.

Chou, C.C., Liu, J.H. and Pham, D.H. (2012), "Steel Buckling-Restrained Braced Frames with Single and Dual Corner Gusset Connections: Seismic Tests and Analyses," *Earthquake Engineering & Structural Dynamics*, pp. 1,137–1,156.

CSI (2011), *User Guide PERFORM-3D: Nonlinear Analysis and Performance Assessment for 3D Structures,* Computers and Structures Inc., Berkeley, CA.

CSI (2013), *CSI Analysis Reference Manual for SAP2000®, ETABS®, SAFE® and CSiBridge®,* Computers and Structures Inc., Berkeley, CA.

Fahnestock, L.A., Sause, R. and Ricles, J.M. (2006), "Analytical and Large-Scale Experimental Studies of Earthquake-Resistant Buckling-Restrained Braced Frame Systems," ATLSS Report No. 06-01.

FEMA (2000), *State of the Art Report on Systems Performance of Steel Moment Frames Subject to Earthquake Ground Shaking,* Federal Emergency Management Agency, Washington DC.

FEMA (2009), *Quantification of Building Seismic Performance Factors,* Report No. FEMA-P695, Applied Technology Council, Redwood City, CA.

Lanning, J., Benzoni, G. and Uang, C.-M. (2016), "Using Buckling-Restrained Braces on Long-Span Bridges I: Full Scale Testing and Design Implications," *Journal of Bridge Engineering*, Vol. 21, No. 5, doi: 10.1061/(ASCE) BE.1943-5592.0000781, 04016001.

Mahin, S., Uriz, P., Aiken, I., Field, C. and Ko, E. (2004), "Seismic Performance of Buckling Restrained Braced Frame Systems," *Proceedings 13th World Conference on Earthquake Engineering,* Vancouver, B.C., Canada, p. 1681.

Sabelli, R. (2001), "Research on Improving the Design and Analysis of Earthquake-Resistant Steel-Braced Frames," Earthquake Engineering Research Institute, Oakland, CA.

SAC (1994), "Suites of Earthquake Ground Motions for Analysis of Steel Moment Frame Structures," retrieved from http://nisee.berkeley.edu/data/strong_motion/sacsteel/ground_motions.html.

Tsai, K.C. and Hsiao, P.C. (2008), "Pseudo-Dynamic Test of a Full-Scale CFT/BRB Frame—Part II: Seismic Performance of Buckling-Restrained Braces and Connections," *Earthquake Engineering & Structural Dynamics*, Vol. 37, No. 7, pp. 1,099–1,115.

Uang, C.M., Nakashima, M. and Tsai, K.C. (2004), "Research and Application of Buckling Restrained Braced Frames," *International Journal of Steel Structures,* Vol. 4, No. 4, pp. 301–313.

Wakabayashi, M., Nakamura, T., Katagihara, A., Yogoyama, H. and Morisono, T. (1973), "Experimental Study on Elastic Plastic Hysteric Behavior of Flat Bar Braces Encased by in Concrete Wall without Bound, Part 1, Preliminary," *Proceedings of the Annual Convention of the Kinki Section of the Architectural Institute of Japan*, pp. 121–144.

Xie, Q. (2005), "State of the Art of Buckling-Restrained Braces in Asia," *Journal of Constructional Steel Research*, Vol. 61, No. 6, pp. 727–748.

Yoshino, T. and Karino, Y. (1971), "Experimental Study on Shear Wall with Braces: Part 2," *Summaries of Technical Papers of Annual Meeting,* Architectural Institute of Japan, Structural Engineering Section, pp. 403–404.

Local Strength of Single-Coped Beams

BO DOWSWELL

ABSTRACT

In beam-to-beam connections, the top flange of the supported beam is usually coped to clear the supporting beam flange. Due to flexural and shear stresses in the coped portion of the web, the local strength can be limited by buckling. Design recommendations in previous editions of the AISC *Manual* imposed limits on the cope geometry and were based on an allowable stress philosophy, limiting the flexural strength to the first-yield moment. To eliminate the limits of applicability and provide equations that take advantage of any available post-yield strength, the design guidance in the 15th Edition AISC *Steel Construction Manual* has been revised from previous editions of the AISC *Manual*. This paper discusses the development of the revised design procedure and validates the equations with the results of 25 experimental tests from five independent research projects.

Keywords: single-coped beams, AISC *Steel Construction Manual*, steel connections, post-yield strength.

INTRODUCTION

In beam-to-beam connections, the top flange of the supported beam is usually coped to clear the supporting beam flange as shown in Figure 1. The cope length can be large at skewed beam connections, connections to wide flange truss chords, and other framing conditions. Due to flexural and shear stresses in the coped portion of the web, the local strength can be limited by buckling.

Design recommendations in previous editions of the AISC *Steel Construction Manual* (AISC, 2011) were developed by Cheng and Yura (1986) based on a local buckling model with an adjustment factor determined by curve fitting data from finite element models. Because the adjustment factor was derived empirically, limits of applicability, based on the maximum cope size modeled, were placed on the design equations. The design procedure is not valid if the cope length exceeds twice the beam depth or the cope depth exceeds 50% of the beam depth. In some practical cases, the cope geometry falls outside these limits of applicability.

Stress concentrations at the reentrant corner, shown in Figure 2, were considered by Cheng and Yura (1986) in the formulation of their equations for web buckling. For flexural yielding calculations, Cheng and Yura recommended that localized yielding due to stress concentrations be neglected. The flexural strength is the minimum of the web buckling moment and the first yield moment. This methodology was common for stress-based design; however, a strength-based design philosophy is now preferred.

To eliminate the limits of applicability and provide equations that take advantage of any available inelastic strength, the design guidance in the 15th Edition *Steel Construction Manual* (AISC, 2017) has been revised from previous editions of the *Manual*. This paper discusses the development of the revised design procedure and validates the equations with the results of 25 experimental tests from five independent research projects.

REVISED DESIGN PROCEDURE

The revised design procedure for the local flexural strength of single-coped beams is on page 9-6 of the 15th Edition *Manual*. The available flexural strength, $\phi_b M_n$ or M_n/Ω_b, of a beam coped at the top flange must equal or exceed the required strength. For beams with compression-flange lateral bracing at the face of the cope, the required flexural strength is:

LRFD	ASD
$M_u = R_u e$ (AISC *Manual* Eq. 9-5a)	$M_a = R_a e$ (AISC *Manual* Eq. 9-5b)

For beams coped at the top flange, the connection element should be located near the coped edge. The minimum length of the connection element is one-half of the coped section depth, h_o. The nominal flexural strength of the coped section is:

When $\lambda \le \lambda_p$

$$M_n = M_p$$

(AISC *Manual* Eq. 9-6)

When $\lambda_p < \lambda \le 2\lambda_p$

$$M_n = M_p - (M_p - M_y)\left(\frac{\lambda}{\lambda_p} - 1\right)$$

(AISC *Manual* Eq. 9-7)

Bo Dowswell, Ph.D., P.E., Principal, ARC International, Birmingham, AL. Email: bo@arcstructural.com

Paper No. 2017-19

When $\lambda_p > 2\lambda_p$

$$M_n = F_{cr} S_{net}$$

(AISC *Manual* Eq. 9-8)

where

$$F_{cr} = \frac{0.903 E k_1}{\lambda^2} \qquad \text{(AISC Manual Eq. 9-9)}$$

$$k_1 = fk \ge 1.61 \qquad \text{(AISC Manual Eq. 9-10)}$$

$$\lambda = \frac{h_0}{t_w} \qquad \text{(AISC Manual Eq. 9-11)}$$

$$\lambda_p = 0.475\sqrt{\frac{k_1 E}{F_y}} \qquad \text{(AISC Manual Eq. 9-12)}$$

The plate buckling coefficient, k, is determined as follows:

When $\dfrac{c}{h_0} \le 1.0$

$$k = 2.2\left(\frac{h_0}{c}\right)^{1.65}$$

(AISC *Manual* Eq. 9-13a)

When $\dfrac{c}{h_0} > 1.0$

$$k = 2.2\frac{h_0}{c}$$

(AISC *Manual* Eq. 9-13b)

The buckling adjustment factor, f, is determined as follows:

When $\dfrac{c}{d} \le 1.0$

$$f = 2\left(\frac{c}{d}\right)$$

(AISC *Manual* Eq. 9-14a)

When $\dfrac{c}{d} > 1.0$

$$f = 1 + \frac{c}{d} \le 3$$

(AISC *Manual* Eq. 9-14b)

where

E = modulus of elasticity, ksi
F_{cr} = critical stress, ksi
F_y = specified minimum yield stress, ksi
M_p = plastic bending moment, kip-in.
= $F_y Z_{net}$
M_y = flexural yield moment, kip-in.
= $F_y S_{net}$
R_a = required end reaction for ASD, kips
R_u = required end reaction for LRFD, kips
S_{net} = elastic section modulus at the cope, in.^{3}
Z_{net} = plastic section modulus at the cope, in.^{3}
c = cope length, in.
d = beam depth, in.
e = distance from the face of the supporting member to the face of the cope, unless a lower value can be justified, in.
f = buckling adjustment factor
h_0 = depth of the coped section, in.
k = plate buckling coefficient
k_1 = modified plate buckling coefficient
t_w = web thickness, in.
λ = web slenderness
λ_p = limiting slenderness for a compact web
Ω_b = 1.67
ϕ_b = 0.90

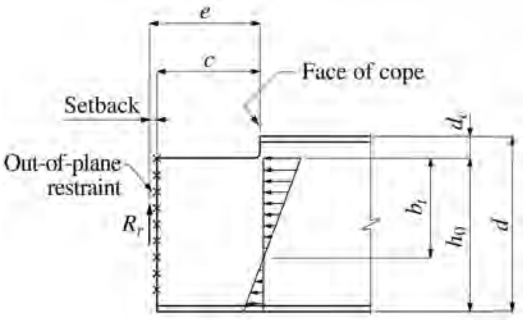

Fig. 1. Single-coped beam.

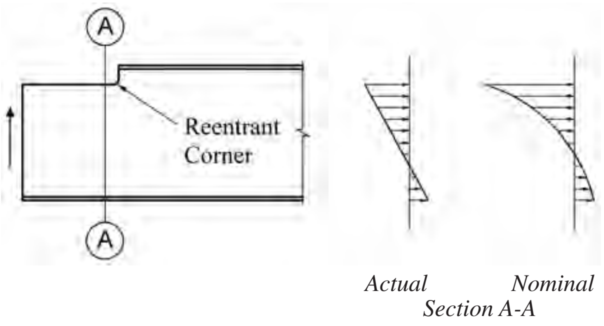

Fig. 2. Local flexural stress at the cope face.

EXISTING RESEARCH

A review of the available research on single-coped beams revealed 25 experimental tests from five previously published research projects. The details of all test specimens are listed in Table A1 of Appendix A, and the experimental results are listed in Tables A2 and A3.

Birkemoe and Gilmor

As part of a larger project, Birkemoe and Gilmor (1978) tested one beam coped at the top flange with bolted clip angles. At the maximum test load, the holes were highly deformed and the tension plane between the bottom bolt and the end of the beam ruptured. Some localized buckling was observed at the top edge of the cope, but it is unclear if the buckling occurred before, or after, the tension-plane rupture.

Ricles and Yura

The results of unpublished experiments by Ricles and Yura are documented in Appendix B of Cheng et al. (1984). The failure mode of all four tests was inelastic web local buckling.

Cheng and Yura

Cheng and Yura (1986) developed the design procedure recommended in previous editions of the AISC *Manual*. The equations were based on the plate buckling model shown in Figure 3, with the flexural stresses idealized using a triangular normal stress distribution along both loaded edges. The top edge was restraint free, and the remaining three edges were fixed against translation but rotationally free. A buckling adjustment factor was developed using a finite element based parametric study that included the effects of stress concentration, shear stress, out-of-plane translation of the reentrant corner, moment gradient over the length of the cope, and rotational restraint of the web at the face of the cope.

Ten experiments were used to verify the design model. Four of the specimens failed by inelastic buckling and six failed by elastic buckling. Compared to these 10 tests along with the four unpublished tests by Ricles and Yura, the equations were shown to be conservative but adequate for design purposes.

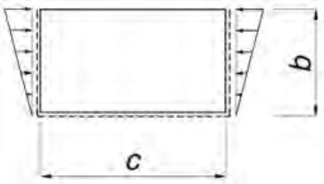

Fig. 3. Plate buckling model.

Yam et al.

Based on a shear buckling model, Yam et al. (2003) developed a set of design equations that accurately predicted the failure loads of four experimental specimens. The critical end reaction is:

$$R_{cr} = \tau_{cr} t_w h_0 \tag{1}$$

The critical shear stress is:

$$\tau_{cr} = \frac{\pi^2 E k_s}{12(1-\nu^2)}\left(\frac{t_w}{h_0}\right)^2 \tag{2}$$

The plate buckling coefficient in shear is:

$$k_s = a\left(\frac{h_0}{c}\right)^b \tag{3}$$

where

$$a = 1.38 - 1.79\left(\frac{d_c}{d}\right) \tag{4}$$

$$b = 1.55 - 3.66\left(\frac{d_c}{d}\right) + 3.64\left(\frac{d_c}{d}\right)^2 \tag{5}$$

k_s = shear buckling coefficient

τ_{cr} = critical shear stress, ksi

ν = Poisson's ratio

Zhong et al.

Zhong et al. (2004) tested 10 single-coped beam specimens with welded clip angles. Four specimens failed in block shear, and six failed in a combined block shear and cope buckling mode. Only the specimens that buckled are included in Table A1.

Discussion

Three failure modes were identified involving local stability of the web: flexural local buckling, shear buckling, and combined block shear and buckling. Most of the observed failure modes were a combination of shear buckling and flexural local buckling, as indicated by buckled shapes that form a diagonal angle between 0° and 45° from vertical. The buckled shapes reported by Cheng et al. (1984) and Yam et al. (2003) were curved, with the angle from vertical increasing with decreasing cope length.

Flexural local buckling is likely to dominate the buckling mode for beams with long copes. With flexural local buckling, the compression edge of the coped section takes the shape of a half sine wave, which usually extends partially into the uncoped portion of the web due to lateral translation of the web at the reentrant corner.

Shear buckling occurs in beams with short cope lengths. Where shear stresses are predominant, the buckled shape is similar to that of the well-documented shear buckling waves in non-coped beams. The buckled shape is characterized by a single wave oriented at an angle of approximately 45° from vertical, as shown in Figure 4.

Combined block shear and cope buckling, hereafter referred to as "block shear buckling," occurs at short copes with shallow end connections as shown in Figure 5. The failure is characterized by a combination of extensive yielding along the L-shape block shear failure pattern, with potential rupture at the tension plane and localized buckling at the face of the cope.

DEVELOPMENT OF DESIGN PROCEDURE

The revised design procedure uses a three-part curve, based on the local buckling design model in the AISC *Specification* (2016). Because the buckled shapes most closely resemble flexural local buckling over the critical variable range, the equations developed by Cheng and Yura (1986) were used for elastic portion of the curve. The limits of applicability are eliminated by transitioning to a minimum plate buckling coefficient, which is not affected by the local stress and restraint conditions due to the large cope dimensions.

Analogy to Local Buckling of Tee Stems

For an infinitely long cope, the strength approaches that of a tee stem in flexural compression. However, there are several differences between tee-beams and copes that can significantly affect the behavior:

- For coped beams, the restraint against twisting of the bottom flange provided by the non-coped portion of the beam creates a fixed boundary condition at the web-to-flange interface.
- The moment gradient over the cope length is higher than for a typical beam.
- The shear load is uniform over the cope length; therefore, both the maximum shear and the maximum moment occur at the face of the cope. Typically, the maximum shear and maximum moment in a tee-beam occur at different locations along the beam length. It is generally expected that the shear load carried by a tee-beam will not affect the flexural strength. Conversely, the experimental research shows that very high shear loads can degrade the flexural strength of copes.
- Extensive yielding of copes does not present a serviceability concern. Due to the high shape factor of tee-beams, AISC *Specification* Section F9.1 imposes an upper limit on the flexural yielding strength.
- The residual stress pattern for coped beams can be much different from that of tee-beams. This will be discussed further in the next section.

Due to these factors, AISC *Specification* Section F9.4 for local buckling of tee stems in flexural compression may not be valid for cope buckling calculations.

Residual Stresses

Residual stresses must be considered in the development of the inelastic segment of the strength curve. Most fabrication operations have an effect on the residual stress pattern, but the last operation performed has the greatest influence on the final pattern.

Copes are usually thermally cut, with grinding if required to remove edge imperfections. Thermal cutting causes tensile residual stresses over a small length at the cut edge (Bjorhovde et al., 2001; Harris, 1997). Residual stresses caused by grinding are dependent on several factors, such as wheel speed, abrasive roughness, and use of coolant. In typical structural fabrication shops, handheld angle grinders are used with no coolant, which induces tensile residual stresses upon cooling (Harvey, 1985).

Tension residual stresses at the cut edge can increase the buckling strength of elements subjected to flexural compression stresses. This effect is clearly demonstrated in the research of Bambach and Rasmussen (2002) and Rogers and Dwight (1977). Unlike the local buckling provisions for noncompact elements in AISC *Specification* Chapter F, which were developed for elements with compression residual stresses, residual stresses for coped beams are beneficial. Therefore, they were neglected in the derivation of AISC *Manual* Equation 9-7.

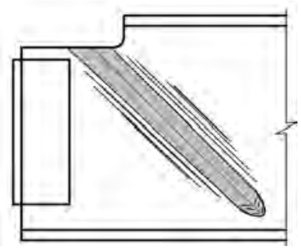

Fig. 4. Shear buckling.

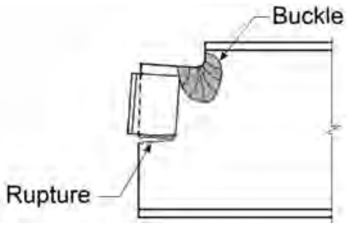

Fig. 5. Block shear buckling.

Buckling Curve

The revised design method uses a three-part curve similar to the local buckling provisions in AISC *Specification* Chapter F. A linear transition between the elastic buckling curve and the plastic strength curve defines the strength when $\lambda_p < \lambda \le \lambda_r$ according to Equation 6:

$$M_n = M_p - (M_p - M_y)\left(\frac{\lambda - \lambda_p}{\lambda_r - \lambda_p}\right) \tag{6}$$

Slenderness Limits

The noncompact slenderness limit, λ_r, can be determined using the critical plate buckling stress according to Equation 7 (Bryan, 1890). For an infinitely long plate with fixed-free boundary conditions at the nonloaded edges and a triangular stress distribution as shown in Figure 3, the plate buckling coefficient, k, is 1.61 (Brockenbrough and Johnston, 1974).

$$\sigma_{cr} = \frac{\pi^2 Ek}{12(1-\nu^2)}\left(\frac{t}{b}\right)^2 \tag{7}$$

where

b = plate width, in.

k = plate buckling coefficient

t = plate thickness, in.

ν = Poisson's ratio

For copes, the width-to-thickness ratio, λ, is defined as h_0/t_w, which is consistent with the AISC *Specification* definition for tee stem buckling. Because only the portion of the web between the neutral axis and the free edge is in compression, this definition is conservative. Based on the current shapes in the AISC *Manual* with the smallest practical cope depth ($d_c = k$), the average value of b_c/h_0 is 0.764, where b_c is the width of the compression region in the web as shown in Figure 1. The standard deviation is 0.0369, and the maximum value of b_c/h_0 for any shape is 0.843.

To estimate the effect of the neutral axis offset, three elastic finite element models of long tee-shaped beams were developed. BASP finite element software was used, as described by Akay et al. (1977), to determine the critical loads. Equal and opposite moments were applied at the ends, and the flange was rotationally fixed against twisting. The cross-sectional dimensions of a W16×26 were used with depths of 8.17 in., 11.17 in. and 14.17 in. The webs buckled in multiple half-wavelengths, indicating that the modeled beam length was appropriate for simulating the behavior of infinitely long copes. Using the current definition for the width-to-thickness ratio ($\lambda = h_0/t_w$), the buckling coefficients calculated with the finite element results are 2.24, 2.34 and 2.42. The average value is 2.33, which is a 45% increase over the theoretical value of 1.61 due to the conservative definition of λ.

Element slenderness values have traditionally been multiplied by a reduction factor, $\alpha = 0.7$, to account for residual stresses and geometric imperfections. Due to the beneficial effect of the residual stress and the conservative definition of λ, $\alpha = 1$ is used in the calculation of the slenderness limit for noncompact webs, λ_r. Using Equation 7, the noncompact limit is

$$\begin{aligned}\lambda_r &= \pi\sqrt{\frac{kE}{12(1-\nu^2)F_y}} \\ &= 0.95\sqrt{\frac{kE}{F_y}}\end{aligned} \tag{8}$$

To account for the differences between cope buckling and plate buckling, the modified plate buckling coefficient, k_1, developed by Cheng and Yura (1986) was substituted for k, resulting in Equation 9.

$$\lambda_r = 0.95\sqrt{\frac{k_1 E}{F_y}} \tag{9}$$

Because $\lambda_p = \lambda_r/2$ provided the best fit to the experimental data, λ_r was replaced with $2\lambda_p$, which allowed Equation 6 to be simplified, resulting in *Manual* Equation 9-7. Limits on the cope length and depth are eliminated by setting the minimum value of k_1 to 1.61 and limiting f to a maximum value of 3.

Experimental Comparisons

Details of 25 experimental tests from five previously published research projects are listed in Appendix A, Table A1. Three failure modes were identified: localized buckling (LB), shear yielding (VY), and block shear buckling (BB). Most of the specimens failing by localized buckling had characteristics of both shear and flexural buckling. Due to the difficulty distinguishing between shear and flexural local buckling, these failure modes were identified as localized buckling. Where further information was available, either elastic localized buckling (EB) or inelastic localized buckling (IB) was identified.

The experimental results for specimens failing by localized buckling or shear yielding are listed in Table A2. Of these 18 specimens, nine failed by elastic buckling, seven failed by inelastic buckling, and two failed by combined shear yielding and inelastic buckling. Table A2 lists the maximum experimental loads and the experimental failure modes. For each specimen, the calculated load is listed for each of the three design procedures discussed: Cheng and Yura (1986), Yam et al. (2003), and the 15th Edition *Manual* procedure. The calculations utilized the measured material and geometric properties where available. Resistance factors and safety factors were omitted from the calculations. For each of the three design procedures, the experimental-to-calculated load ratio, R_e/R_c, and predicted failure mode are listed. All three design procedures are reasonably accurate.

In most cases, the revised AISC *Manual* design procedure accurately predicted the experimental failure mode. For the specimens failing in elastic localized buckling, the revised *Manual* procedure and the Cheng and Yura (1986) method produce identical results. The primary difference between the two methods is with the more common case of inelastic localized buckling, where the revised *Manual* equations are more accurate and less conservative. The average experimental-to-calculated load ratio for the revised *Manual* procedure is 1.23 with a standard deviation is 0.267.

The experimental data is plotted in Figure 6 with the three-part curve defined by the revised AISC *Manual* design procedure. Due to the high slenderness of Cheng and Yura's (1986) specimens PB26A and PB26B, the data points fall outside of the range of Figure 6. For the specimens predicted to fail by shear yielding, the vertical-axis values were calculated using an equivalent plastic moment, $M_p = V_y e$, where V_y is the shear yield force calculated with AISC *Specification* Equation J4-3 using the measured material and geometric properties. The experimental data follow the design curve for moderate and high slenderness values; however, three data points fall slightly below the curve in the low-slenderness range. This is caused by the interaction of shear and normal loads, which has the greatest effect on the specimens with short cope lengths, where λ approaches λ_p.

Influence of Inflection Point Location

To reflect the standard practice of neglecting any effect of connection rotational rigidity on the cope strength, e is defined as the "distance from the face of the supporting member to the face of the cope…" However, the second part of the definition, "…unless a lower value can be justified," allows the engineer to determine if a smaller value is appropriate. Because the plate buckling equations developed by Cheng and Yura (1986) include the effects of shear stress and moment gradient over the length of the cope, the validity of calculating the required moment based on an inflection point within the cope (Figure 7) is questionable. Cheng and Yura's (1986) specimens W3 and RB18A illustrate this point.

Specimen W3 had an inflection point 3.9 in. from the beam end (Table A2 in Appendix A), which is 37% of the cope length. With a local slenderness ratio, $\lambda/\lambda_p = 1.51$, as predicted, the specimen failed by inelastic localized buckling. As listed in Table A2, the AISC *Manual* design procedure is 10% conservative when the influence of the inflection point location is neglected. If the required moment is calculated using the actual location of the inflection point, the calculated load is nonconservative, with an experimental-to-calculated load ratio of $R_e/R_c = 0.830$.

For specimen RB18A, the inflection point was 8 in. from the beam end (Table A2 in Appendix A), which is 44% of the cope length. With a local slenderness ratio, $\lambda/\lambda_p = 1.74$, as predicted, the specimen failed by inelastic localized buckling. As listed in Table A2, the AISC *Manual* design

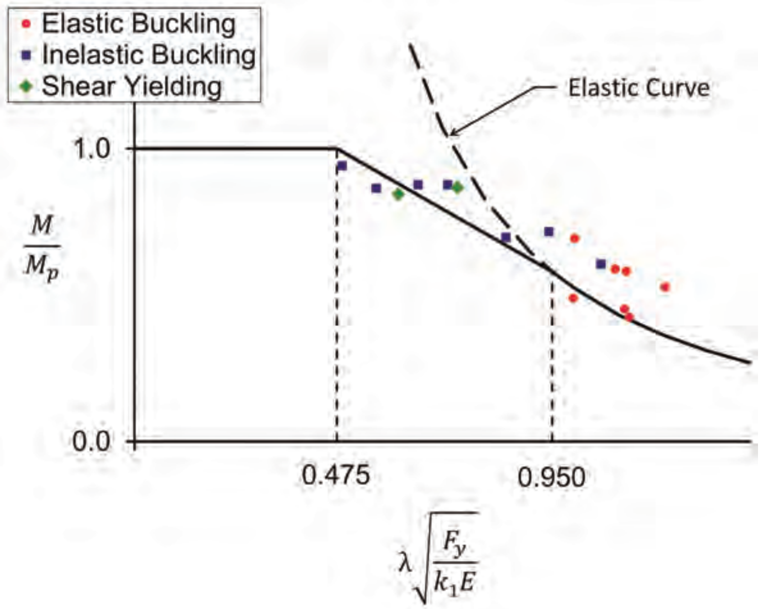

Fig. 6. Normalized moment versus normalized slenderness.

procedure is 27% conservative when the effect of the inflection point is neglected. If the required moment is calculated using the actual location of the inflection point, the calculated load is nonconservative, with an experimental-to-calculated load ratio of $R_e/R_c = 0.600$.

Based on the λ/λ_p ratios, it appears that the inflection point location has a greater effect on less slender copes. Until further research is available, the following design guidance is suggested:

- Generally, e should be defined as the distance from the face of the cope to the end of the beam.
- When $\lambda \leq \lambda_p$, the required moment can be calculated using the inflection point location.
- When $\lambda > \lambda_p$, the required moment can be calculated using the inflection point location only if an additional check is made for shear buckling according to Equations 1 through 5.

Block Shear Buckling

The seven specimens that failed by block shear buckling are documented in Table A3. Using the revised AISC *Manual* procedure and *Specification* Sections J4.2 and J4.3, the strength of each specimen was calculated for the limit states of flexure, shear yielding, and block shear. The calculated beam reactions for each of the three limit states are listed in columns 4 through 6, and the minimum of the three calculated values, R_{min}, is listed in column 7. The calculations utilized the measured material and geometric properties where available. Resistance factors and safety factors were omitted from the calculations. For all specimens, the calculated strength was controlled by block shear.

The experimental-to-calculated load ratios, R_e/R_{min}, are listed in column 8 of Table A3. The average experimental-to-calculated load ratio is 1.03 with a standard deviation of 0.126. Although the average value is greater than 1.00, the reliability of this failure mode is lower than for other coped beams failing in a traditional block shear mode with no cope buckling. For coped beams with welded clip angles failing in block shear with no buckling, the average experimental-to-calculated load ratio is 1.24 with a standard deviation of 0.0847. For coped beams with single-row bolted clip angles failing in block shear with no buckling, the average experimental-to-calculated load ratio is 1.37 with a standard deviation of 0.121.

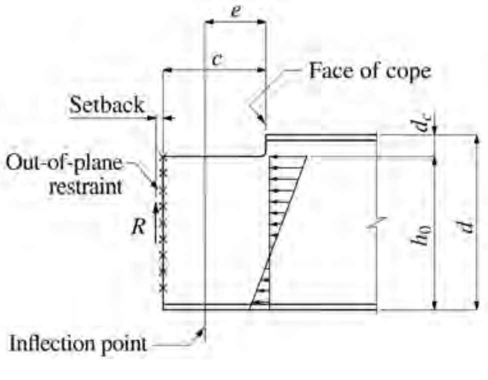

Fig. 7. Eccentricity defined by the inflection point.

Because all of the specimens failing by block shear buckling had a short connection element depth, L, compared to the depth of the coped section, h_0, it is believed that this failure mode can be eliminated by satisfying $L/h_0 \geq 0.5$. As shown in column 2 of Table A3, the L/h_0 values for all specimens are less than 0.5. For most practical connections this requirement is satisfied by the AISC *Manual* recommendation for erection stability, where the minimum angle length is equal to one-half of the beam T-dimension.

CONCLUSIONS

Results from five previously published research projects were used to develop design recommendations for single-coped beams that are consistent with strength design philosophy. The revised design method, which is included in the 15th Edition AISC *Steel Construction Manual* (AISC, 2017), uses a three-part curve similar to the local buckling provisions in AISC *Specification* Chapter F (AISC, 2016). The limitations on cope length and cope depth in the previous *Manual* design procedure are not required with the revised procedure.

For long, slender copes that are controlled by elastic buckling, and for copes that are controlled by shear yielding, the revised design procedure results in the same strength as the previous *Manual* procedure. However, the revised equations utilize the inelastic flexural strength of nonslender copes, which reduces the conservatism and improves the accuracy compared to the previous AISC *Manual* equations.

Of the 25 experiments evaluated, 18 specimens failed by either localized buckling or shear yielding. In most cases, the revised design procedure accurately predicted the experimental failure mode. The average experimental-to-calculated load ratio for the 15th Edition AISC *Manual* procedure is 1.23 with a standard deviation is 0.267.

A new failure mode that combined block shear and cope buckling (block shear buckling) occurred in seven experimental specimens with short copes and shallow end connections. To prevent this limit state, a new geometric limit requires the connection element at the beam end to be at least one-half of the coped section depth.

DESIGN EXAMPLE

Given: Using LRFD design, determine if the cope flexural strength is adequate for a 70-kip factored beam end reaction for the beam shown in Figure 8. The beam material is ASTM A992.

Solution:

From AISC Manual Table 1-1:

W18×35
$t_w = 0.30$ in. $d = 17.7$ in.

From AISC *Manual* Table 9-2: $S_{net} = 18.2 \text{ in.}^3$

From AISC Design Examples V15.0 Table IV-11: $Z_{net} = 32.1 \text{ in.}^3$

$$\begin{aligned} M_y &= F_y S_{net} \\ &= (50 \text{ ksi})(18.2 \text{ in.}^3) \\ &= 910 \text{ kip-in.} \end{aligned}$$

$$\begin{aligned} M_p &= F_y Z_{net} \\ &= (50 \text{ ksi})(32.1 \text{ in.}^3) \\ &= 1{,}610 \text{ kip-in.} \end{aligned}$$

$$\begin{aligned} \frac{c}{d} &= \frac{7.5 \text{ in.}}{17.7 \text{ in.}} \\ &= 0.424 \end{aligned}$$

Because $\dfrac{c}{d} < 1.0$, AISC *Manual* Equation 9-14a is applicable:

$$\begin{aligned} f &= 2\left(\frac{c}{d}\right) \\ &= 2(0.424) \\ &= 0.847 \end{aligned}$$

$$\begin{aligned} \frac{c}{h_0} &= \frac{7.5 \text{ in.}}{15.7 \text{ in.}} \\ &= 0.478 \end{aligned}$$

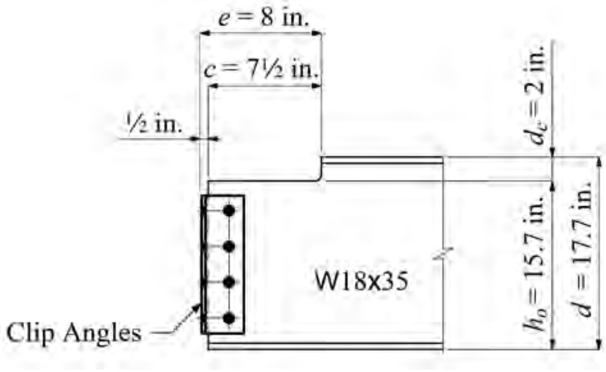

Fig. 8. Design example.

Because $\dfrac{c}{h_0} < 1.0$, AISC *Manual* Equation 9-13a is applicable:

$$\begin{aligned}
k &= 2.2\left(\frac{h_0}{c}\right)^{1.65} \\
&= 2.2\left(\frac{15.7}{7.5}\right)^{1.65} \\
&= 7.44
\end{aligned}$$

$$\begin{aligned}
k_1 &= fk \geq 1.61 \\
&= (0.847)(7.44) \\
&= 6.30
\end{aligned}$$

$$\begin{aligned}
\lambda &= \frac{h_o}{t_w} \\
&= \frac{15.7\text{ in.}}{0.300\text{ in.}} \\
&= 52.3
\end{aligned}$$

$$\begin{aligned}
\lambda_p &= 0.475\sqrt{\frac{k_1 E}{F_y}} \\
&= 0.475\sqrt{\frac{(6.30)(29{,}000\text{ ksi})}{(50\text{ ksi})}} \\
&= 28.7
\end{aligned}$$

Because $\lambda_p < \lambda \leq 2\lambda_p$, AISC *Manual* Equation 9-7 is applicable.

$$\begin{aligned}
M_n &= M_p - (M_p - M_y)\left(\frac{\lambda}{\lambda_p} - 1\right) \\
&= 1{,}610\text{ kip-in.} - (1{,}610\text{ kip-in.} - 910\text{ kip-in.})\left(\frac{52.3}{28.7} - 1\right) \\
&= 1{,}030\text{ kip-in.}
\end{aligned}$$

$$\begin{aligned}
\phi R_n &= \frac{\phi M_n}{e} \\
&= \frac{(0.90)(1{,}030\text{ kip-in.})}{8\text{ in.}} \\
&= 116\text{ kips} > 70\text{ kips} \quad \textbf{o.k.}
\end{aligned}$$

Therefore, the W18×35 coped beam is adequate to resist the 70-kip end reaction.

SYMBOLS

A_{gv}	Gross area subjected to shear, in.^{2}
E	Modulus of elasticity, ksi
F_{cr}	Critical stress, ksi
F_y	Specified minimum yield stress, ksi
L	Connection element depth, in.
M_a	Required flexural strength for ASD, kip-in.
M_p	Plastic bending moment, kip-in.
M_u	Required flexural strength for LRFD, kip-in.
M_y	Flexural yield moment, kip-in.
R_a	Required end reaction for ASD, kips
R_r	Required end reaction, kips

R_u	Required end reaction for LRFD, kips
S_{net}	Elastic section modulus at the cope, in.^{3}
V_n	Nominal shear yield force, kips
V_r	Required shear force, kips
V_y	Shear yield force calculated with the measured material and geometric properties, kips
Z_{net}	Plastic section modulus at the cope, in.^{3}
b	Plate width, in.
b_c	Width of the compression region in the web, in.
c	Cope length, in.
d	Beam depth, in.
d_c	Cope depth, in.
e	Distance from the face of the supporting member to the face of the cope, unless a lower value can be justified, in.
f	Buckling adjustment factor
h_0	Depth of the coped section, in.
k	Plate buckling coefficient
k_s	Shear buckling coefficient
k_1	Modified plate buckling coefficient
s	Web depth dedicated to shear resistance, in.
t	Plate thickness, in.
t_f	Flange thickness, in.
t_w	Web thickness, in.
y_p	Distance from the bottom of the beam to the plastic neutral axis, in.
λ	Web slenderness
λ_p	Limiting slenderness parameter for a compact element
λ_r	Limiting slenderness parameter for a noncompact element
Ω_b	Safety factor for flexure
Ω_v	Safety factor for shear yielding
ϕ_b	Resistance factor for flexure
ϕ_v	Resistance factor for shear yielding
τ_{cr}	Critical shear stress, ksi
ν	Poisson's ratio

REFERENCES

AISC (2011), *Steel Construction Manual*, 14th Edition, American Institute of Steel Construction, Chicago, IL.

AISC (2016), *Specification for Structural Steel Buildings*, ANSI/AISC 360-16, American Institute of Steel Construction, Chicago, IL.

AISC (2017), *Steel Construction Manual*, 15th Edition, American Institute of Steel Construction, Chicago, IL.

Akay, H.U., Johnson, C.P. and Will, K.M. (1977), "Lateral and Local Buckling of Beams and Frames," *Journal of the Structural Division,* ASCE, Vol. 103, No. ST9, pp. 1,821–1,832.

Bambach, M.R. and Rasmussen, K.J.R. (2002), "Tests of Unstiffened Elements Under Combined Compression and Bending," Research Report R818, Center for Advanced Structural Engineering, University of Sydney.

Birkemoe, P.C. and Gilmor, M.I. (1978), "Behavior of Bearing Critical Double-Angle Beam Connections," *Engineering Journal*, AISC, Vol. 15 , No. 4, pp. 109–115.

Bjorhovde, R., Engstrom, M.F., Griffis, L.G., Kloiber, L.A. and Malley, J.O. (2001), *Structural Steel Selection Considerations—A Guide for Students, Educators, Designers, and Builders*, American Society of Civil Engineers, Reston, VA.

Brockenbrough, R.L. and Johnston, B.G. (1974), *U.S. Steel Design Manual*, 2nd Edition, U.S. Steel Corporation, Pittsburgh, PA.

Bryan, G.H. (1890), "On the Stability of a Plane Plate under Thrusts in Its Plane, with Applications to the Buckling of the Sides of a Ship," *Proceedings of the London Mathematical Society*, Vol. 22, No. 1, pp. 54–67.

Cheng, J.J. and Yura, J.A. (1986), "Local Web Buckling of Coped Beams," *Journal of Structural Engineering*, ASCE, Vol. 112, No. 10.

Cheng, J.J., Yura, J.A. and Johnson, C.P. (1984), "Design and Behavior of Coped Beam," Ferguson Lab Report, University of Texas at Austin, Austin, TX.

Harris, I.D. (1997), *Plasma Arc Cutting of Bridge Steels*, Report 384, National Cooperative Highway Research Program, National Academy Press, Washington, DC.

Harvey, J.F. (1985), *Theory and Design of Pressure Vessels*, Van Nostrand Reinhold Co., New York, NY.

Rogers, N.A. and Dwight, J.B. (1977), "Outstand Strength," *Steel Plated Structures, An International Symposium*, Granada Publishing LTD.

Yam, M.C.H., Lam, A.C.C., Lu, V.P. and Cheng, J.J.R. (2003), "Local Web Buckling Strength of Coped Steel I Beams," *Journal of Structural Engineering*, ASCE, Vol. 129, No. 1.

Zhong, J.Y.C., Yam, M.C.H., Lam, A.C.C. and Iu, V.P. (2004), "Experimental Investigation of Block Shear of Coped Beams with Welded Clip Angles Connection," *Proceedings, Fifth Structural Specialty Conference of the Canadian Society for Civil Engineering,* June 2–5.

APPENDIX A. TABLES

Table A1. Specimen Properties

Specimen	F_y (ksi)	E (ksi)	d (in.)	b_f (in.)	t_f (in.)	t_w (in.)	e (in.)	d_c (in.)	c (in.)
Cheng and Yura (1986)									
W1	39.4	29000[a]	17.9	6.00	0.439	0.304	4.00	1.25	3.50
W2	39.4	29000[a]	17.9	6.00	0.439	0.304	7.00	1.25	6.50
W3	39.4	29000[a]	17.9	6.00	0.439	0.304	10.5	1.25	10.0
RB18A	39.4	29000[a]	17.9	6.00	0.439	0.304	18.2	3.06	18.0
RB12A	57.3	29000[a]	11.9	3.97	0.239	0.212	9.09	1.25	8.90
RB12D	57.3	29000[a]	11.9	3.97	0.239	0.212	18.0	3.13	17.9
RB12B	55.3	29000[a]	12.0	4.00	0.239	0.217	12.2	1.13	12.0
RB12C	55.3	29000[a]	12.0	4.00	0.239	0.217	18.3	1.00	18.1
PB26A	59.4	29000[a]	26.5	6.00	0.181	0.132	13.1	1.13	13.0
PB26B	59.4	29000[a]	26.5	6.00	0.181	0.132	8.29	0.91	8.16
Ricles and Yura (Ref: Cheng and Yura, 1986)									
10–4	50.3	29000[a]	9.9	5.70	0.360	0.251	8.50	1.50	8.00
10–7	50.3	29000[a]	9.9	5.70	0.360	0.251	6.50	1.75	6.00
18–14	36.6	29000[a]	18.2	7.47	0.685	0.423	9.00	1.50	8.00
18–15	36.6	29000[a]	18.2	7.47	0.685	0.423	5.63	1.50	5.00
Yam et al. (2003)									
406d005	49.7	31400	15.7	5.50[a]	0.345[a]	0.250[a]	13.7	0.78	13.5
406d01	49.7	31400	15.7	5.50[a]	0.345[a]	0.250[a]	13.7	1.57	13.5
406d03	49.7	31400	15.7	5.50[a]	0.345[a]	0.250[a]	13.7	4.70	13.5
457d02	49.7	31400	17.7	6.00[a]	0.425[a]	0.300[a]	15.5	3.54	15.3
Birkemoe and Gilmor (1978)									
I-2	52.5	29000[a]	18.0[a]	7.50[a]	0.500[a]	0.305[a]	6.50	1.00	6.00
Zhong et al. (2004)									
A1	46.1	27700	15.9	5.55	0.437	0.268	5.12	1.29	3.94
A2	46.1	27700	15.9	5.55	0.437	0.268	5.91	1.22	4.73
B1	46.1	27700	15.9	5.55	0.437	0.268	5.12	1.18	3.94
B2	46.1	27700	15.9	5.55	0.437	0.268	6.30	1.18	5.12
D1	53.9	29500	18.0	7.45	0.559	0.362	7.09	1.18	5.91
E2	42.4	29500	14.3	6.75	0.598	0.358	5.12	1.18	3.94

[a] Nominal value

Table A2. Specimens Failing by Localized Buckling or Shear Yielding

	Experiment		Cheng and Yura (1986)			Yam et al. (2003)			15th Ed. AISC Manual		
Specimen	R_e (kips)	EFM	R_c (kips)	$\frac{R_e}{R_c}$	PFM	R_c (kips)	$\frac{R_e}{R_c}$	PFM	R_c (kips)	$\frac{R_e}{R_c}$	PFM
Cheng and Yura (1986)											
W1	115	VY/IB	119	0.966	VY	119	0.966	VY	119	0.966	VY
W2	112	VY/IB	115	0.966	FY	119	0.935	VY	119	0.935	VY
W3[a]	99.0	IB	76.9	1.29	FY	109	0.905	LB	89.5	1.11	IB
RB18A[b]	46.5	IB	36.0	1.29	FY	43.2	1.08	LB	36.5	1.27	IB
RB12A	37.9	IB	28.8	1.32	LB	34.9	1.09	LB	28.8	1.32	EB
RB12D	12.9	EB	9.10	1.42	LB	13.4	0.959	LB	9.10	1.42	EB
RB12B	27.8	EB	20.6	1.35	LB	26.3	1.06	LB	20.6	1.35	EB
RB12C	16.8	EB	11.5	1.46	LB	15.7	1.07	LB	11.5	1.46	EB
PB26A	14.1	EB	6.88	2.05	LB	7.97	1.77	LB	6.88	2.05	EB
PB26B[c]	20.8	EB	14.9	1.39	LB	16.1	1.29	LB	14.9	1.39	EB
Ricles and Yura (Ref: Cheng and Yura, 1986)											
10–4	47.0	IB	27.9	1.68	FY	57.8	0.813	LB	38.9	1.21	IB
10–7	59.0	IB	34.5	1.71	FY	62.0	0.953	VY	51.7	1.14	IB
18–14	151	IB	122	1.24	FY	155	0.973	VY	155	0.973	VY
18–15	164	IB	155	1.06	VY	155	1.061	VY	155	1.06	VY
Yam et al. (2003)											
406d005	37.3	EB	35.3	1.06	LB	44.1	0.845	LB	35.3	1.06	EB
406d01	36.2	EB	32.6	1.11	LB	39.9	0.907	LB	32.6	1.11	EB
406d03	25.2	EB	25.5	0.988	LB	28.5	0.883	LB	25.5	0.988	EB
457d02	60.5	EB	43.5	1.39	LB	51.1	1.18	LB	43.5	1.39	EB
			Average	1.32			1.04			1.23	
			Standard deviation	0.288			0.218			0.267	

[a] For specimen W3, the inflection point was 3.9 in. from the beam end. Clip angles restrained buckling.

[b] For specimen RB18A, the inflection point was 8 in. from the beam end.

[c] Specimen PB26B failed by shear buckling with post-buckling capacity due to tension field action.

R_e = experimental beam end reaction

R_c = calculated beam end reaction

EFM: experimental failure mode
PFM: predicted failure mode

EB: elastic localized buckling
FY: flexural yielding
IB: inelastic localized buckling
LB: localized buckling
VY: shear yielding

Table A3. Specimens Failing by Block Shear Buckling

Specimen	L/h_o	R_e (kips)	R_f (kips)	R_v (kips)	R_b (kips)	R_{min} (kips)	$\frac{R_e}{R_{min}}$
Birkemoe and Gilmor (1978)							
I-2[a]	0.353	112	220	163	122	122	0.918
Zhong et al. (2004)							
A1	0.431	88.8	177	108	86.3	86.3	1.03
A2	0.375	98.3	146	109	94.0	94.0	1.05
B1	0.321	88.6	179	109	74.6	74.6	1.19
B2	0.294	87.7	134	109	98.8	98.8	0.888
D1	0.282	140	279	196	155	155	0.903
E2	0.360	131	239	119	107	107	1.22
						Average	1.03
						Standard deviation	0.126

[a] The bolt bearing strength for specimen I-2, according to AISC Specification Equation J3-6b, is 163 kips.

R_e = experimental beam end reaction
R_f = calculated beam end reaction for the limit state of flexure, based on the revised AISC *Manual* design procedure
R_v = calculated beam end reaction for the limit state of shear yielding
R_b = calculated beam end reaction for the limit state of block shear
R_{min} = minimum of R_f, R_v and R_b

Steel Structures Research Update

Seismic Performance and Design of Steel Panel Dampers for Steel Moment Frames

JUDY LIU

INTRODUCTION

Ongoing work on the seismic performance and design of steel panel dampers for steel moment frames is highlighted. Dr. Keh-Chyuan Tsai, professor in the Department of Civil Engineering at National Taiwan University, leads the team from National Taiwan University and the National Center for Research on Earthquake Engineering (NCREE) in Taipei. In 2018, Dr. Tsai received an AISC Special Achievement Award in recognition of "extensive work with U.S. researchers to conduct large-scale system level testing of structural steel seismic force resisting systems, leading to system level verification of many of the AISC 341 provisions" (AISC, 2018).

At NCREE, one recent collaboration with the University of Washington included cyclic tests of a three-story chevron special concentrically braced frame (SCBF). Current seismic design provisions require large beam sizes to resist the unbalanced forces from the chevron braces after brace buckling. The research has explored options for alternative ductile mechanisms and reduced beam sizes. The three-story tests followed a series of one-story frame tests, demonstrating that beam yielding following brace buckling "improved the deformability of the SCBF without compromising the capacity of the system," and highlighting limitations with respect to weak beams (NCREE, 2018). The three-story tests were used to validate finite element models and to further inform proposed design requirements for the AISC *Seismic Provisions.*

Steel research at NCREE has also included studies on steel beam-to-box-column moment connections and electro-slag-welded (ESW) joints in those connections. Cyclic tests on full-scale, welded beam-to-box-column connections showed inadequate strength and ductility as a result of diaphragm plates that had not been properly welded to the columns (Tsai et al., 2015). Tsai et al. (2015) developed recommendations for improved design, fabrication and inspection procedures. Meanwhile, research into premature fracture of ESW diaphragm-to-column joints in beam-to-box-column connections has revealed sensitivity to eccentricity in loading between the beam flange and the diaphragm. Further, a micromechanical-based stress-modified critical stress (SMCS) model has been developed and shown to be capable of predicting the crack initiation of the diaphragm-to-column ESW joint (Li et al., 2018).

The steel panel damper research described here complements a variety of studies around the world focused on providing supplemental energy dissipation for improved seismic performance. From Argentina, the multiple friction damper (MFD) is composed of friction elements that can be stacked around an existing column to dissipate energy with horizontal movement of the column (Martinez and Curadelli, 2017). In China, the curved surfaces of the arc-surfaced frictional damper (AFD) in a diagonal brace, for example, result in damping forces that vary with displacement (Wang et al., 2017). Korean researchers have combined a steel slit damper and rotational friction dampers for seismic retrofit of a reinforced concrete (RC) moment frame with core walls (Lee et al., 2017) and have also explored a set of steel slit dampers assembled into a box shape and used in knee braces for retrofit of an RC moment frame (Lee and Kim, 2017). The steel panel dampers utilize a different mechanism but share the common goal of reducing deformation and force demands on the system.

RESEARCH OBJECTIVES

Motivated in part by the 1995 Great Hanshin-Awaji earthquake, researchers have sought methods to improve the performance of seismic-force-resisting systems such as steel moment-resisting frames (MRFs). Among the methods explored were low-yield-stress steel shear panel dampers, shown by Liu et al. (2007), Otani et al. (2001), and Tanaka and Sasaki (2000) to provide good energy dissipation capacity. Contemporary work by Tsai et al. (2001) demonstrated through substructure pseudodynamic tests and analysis that low-yield steel shear panel dampers as additional Vierendeel frame "columns" improved performance by exhibiting "excellent energy dissipation characteristics thereby reducing the inelastic deformational demand imposed on the beam-to-column connections in the conventional MRFs."

Tsai et al. (2018) have developed the steel panel damper

Judy Liu, Ph.D., Research Editor of the AISC *Engineering Journal*, Professor, Oregon State University, School of Civil & Construction Engineering, Corvallis, OR. Email: judy.Liu@oregonstate.edu

(SPD) incorporated into a SPD-MRF as shown in Figure 1. The SPD features three segments: a middle inelastic core (IC) with buckling-restraining stiffeners and two elastic joint (EJ) segments top and bottom. The three segments are fabricated from two different I-sections, with the two EJ segments using the same, stronger section. All segments are rigidly connected to each other and to the boundary beams and remain elastic in a service level earthquake (SLE). The inelastic core (IC) is expected to see inelastic shear deformations in a design basis earthquake (DBE) or maximum considered earthquake (MCE) and to dissipate energy through significant inelastic shear deformations in a severe earthquake. Shear buckling at large deformations is prevented by the stiffeners.

Much of the SPD-related research to date has focused on the behavior, design and detailing of the inelastic core (IC), or shear panel (e.g., Chen et al., 2006). Information on the seismic performance of SPD-MRFs is lacking, as are comprehensive guidelines for seismic design of the three-segment SPDs and the SPD-MRF. The overarching goal of the research has been to fill the knowledge gaps, and Tsai et al. (2018) have accomplished this through testing of two full-scale SPD specimens and numerical simulations using Abaqus and PISA3D. Specifically, for SPD-MRF design and evaluation, research objectives are to provide procedures for design of the IC segment; to develop capacity design methods (CDM) for the EJ segments, boundary beams, and the SPD-to-beam panel zones; and to develop numerical models, including a three-segment SPD model and an equivalent one-element model.

SEISMIC DESIGN WITH STEEL PANEL DAMPERS

The performance objectives for the SPD and SPD-MRF include the requirement that all elements remain elastic in an SLE, that the inelastic shear deformations are concentrated in the inelastic core (IC) for a DBE or MCE, and that the SPD is able to dissipate energy through significant inelastic shear deformations in the MCE. SPD design and detailing requirements, including details of the buckling-restraining stiffeners in the IC, have been developed. Capacity design methods (CDM) for the elastic joints (EJ) and the boundary beams have also been developed.

Seismic Design of SPDs

The design of the SPD centers on the energy-dissipating IC, which has a thinner or weaker web than the EJ segments. The flanges of the SPD are considered to be continuous over the three segments. The strength of the SPD is governed by shear yielding of the IC, assuming axial load effects to be insignificant. The SPD stiffness can be adjusted by changing the relative heights of the two identical EJ and of the IC, as well as by stiffening the EJ.

Capacity design of the EJ is achieved by considering the shear and moment expected from full shear yielding of the IC. Shear demands on the EJ are calculated with the shear yield strength using the expected yield stress, R_yF_y, and a strain-hardening factor for the web of the IC. For calculation of the corresponding maximum EJ moment demands, an inflection point is assumed at mid-height of the SPD. Though the proposed approach does not consider shear-moment interaction, Tsai et al. (2018) also propose an alternative, more conservative approach with calculations of von Mises stresses.

The web and end stiffeners of the IC (Figure 1) delay the onset of shear buckling to maximize energy dissipation in the case of severe earthquakes. Design and detailing of the stiffeners follow the requirements developed by Chen et al. (2006). The end stiffeners are full depth, are welded to the SPD flanges, and form the boundaries between the IC and the EJ. The IC and EJ webs are welded to either side of an end stiffener. Vertical and horizontal web, or buckling-restraining, stiffeners can be welded to opposite sides of the web. These web stiffeners are also welded to the end stiffeners or SPD flanges, as applicable. Spacing of the IC

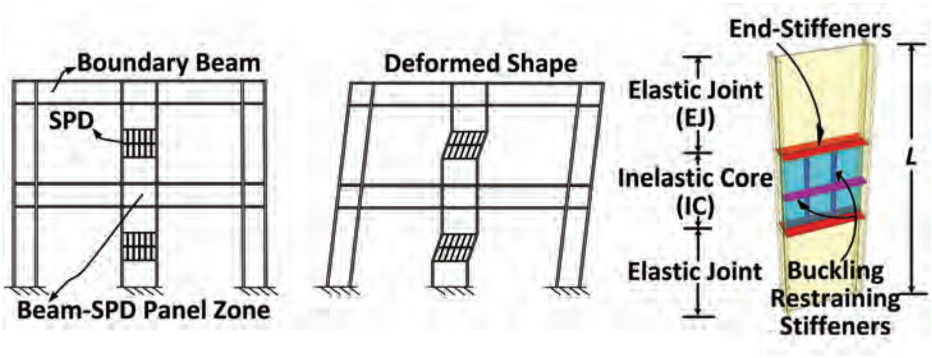

Fig. 1. Schematics of SPD and SPD-MRF.

web stiffeners is chosen to satisfy the recommended limits on slenderness of the web between stiffeners (Chen et al., 2006). All stiffeners are sized to delay out-of-plane buckling using a rigidity requirement developed by Chen et al. (2006). The end and horizontal web stiffeners are also sized for axial force demands from shear buckling and the development of tension field action in the IC web so as to "resist the pull-in forces" on the IC flanges (Tsai et al., 2018).

For calculations of SPD lateral stiffness in cases with no rotation at the boundary beams, Tsai et al. (2018) provide an equation that includes the shear and bending stiffnesses of the IC and EJ segments. The equation can be used for the SPD post-yield stiffness by modifying the shear modulus for the IC by a strain hardening ratio as adopted for a bilinear material stress-strain relationship.

Seismic Design of Steel MRFs with SPDs

Seismic design of SPD-MRF requires capacity design of the boundary beams and of the SPD-to-beam panel zones. As for ductile design of conventional MRF, inelastic behavior in the beams should be restricted to the ends, at the beam-to-column connections. Recommendations for capacity design of the boundary beams are based on seismic provisions to prevent shear or flexural yielding in the beam outside the link in eccentrically braced frames (AISC, 2016). Similarly, the SPD-to-beam panel zones are capacity designed to avoid shear yielding for the expected demands. Additional recommendations for seismic design of SPD-MRF can be found in Tsai et al. (2018).

TEST PROGRAM

Validation of some of the proposed seismic design procedures was achieved through cyclic testing of two, full-scale SPD specimens. Different stiffener details were explored, and the ductile behavior of the SPD was confirmed.

Test Specimens

The two full-scale, 8.53-ft-tall SPD specimens, SPD-2L0T and SPD-2L1T, were identical other than an additional horizontal stiffener for specimen SPD-2L1T [Figure 2(a)]. Each specimen had a 3.94-ft-tall IC and 2.30-ft-tall EJs. The I-sections had overall depth and width of 23.6 in. and 9.84 in., respectively, and 1.18-in.-thick flanges of SN490B (approximately 47-ksi yield stress) steel. The EJ webs were 0.866-in.-thick SN490B steel. The IC webs were 0.315-in.-thick SN400B (approximately 34-ksi yield stress) steel. Properties adopted for the SN400B IC webs included an expected yield stress ratio, R_y, of 1.3 and a strain-hardening factor, ω, of 1.5. SN490B stiffeners included a pair of 0.472-in. × 3.94-in. vertical stiffeners on one side and one 0.984-in. × 3.94-in. horizontal stiffener on the other side of the web for specimen SPD-2L1T. As shown in Figure 2(a), 15.7-in. tall T-shaped stiffeners were added to stiffen the top and bottom end plates used to secure the test specimen to the testing system. Additional details of the test specimens can be found in Tsai et al. (2018).

Test Setup and Loading

NCREE's multiaxial testing system (MATS) was used to apply lateral displacements without rotation or net vertical force, as shown in Figure 2(b). Load cells in the servohydraulic actuators provided forces for determination of shear and bending in the SPD specimens. Displacement transducers [noted as LVDT in Figure 2(b)], tilt meters, and dial gauges were used to determine lateral translations and rotations at top and bottom of the IC and of the SPD. The displacement history followed the cycles of increasing lateral drift as required for cyclic tests for qualification of beam-to-column connections (AISC, 2016).

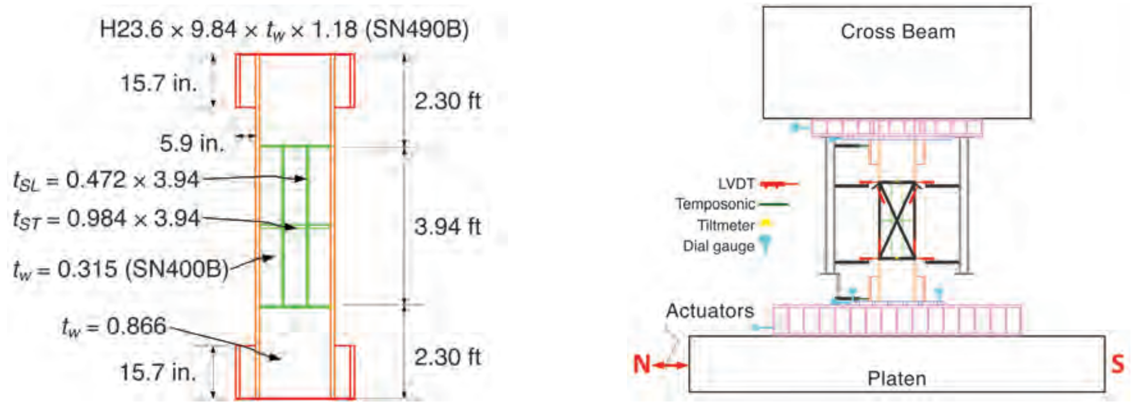

(a) *(b)*

Fig. 2. (a) Details of SPD specimens and (b) test setup.

Experimental Results

The test results validated proposed SPD design procedures. The EJ in both specimens remained elastic throughout the tests. The IC stiffeners effectively delayed shear buckling in the web, and both specimens dissipated energy without apparent strength or stiffness degradation beyond 4% interstory drift (Figure 3). Note that the shear deformations were on the order of 0.11 rad before failure. Specimen SPD-2L0T failed in the first cycle of 5% interstory drift, as can be seen in Figure 3(b), with a fracture that had initiated near a stiffener-to-web weld. Specimen SPD-2L1T failed in the second cycle at 5% interstory drift as shown in Figure 3(a). The slightly larger deformation capacity of SPD-2L1T (a 3% increase in the cumulative plastic deformation capacity) was attributed to the addition of the transverse stiffener. Overall, the shear-deformation response was similar, as shown in Figure 3(c).

NUMERICAL MODELS

Two types of computational models—a shell element model (Abaqus) and a frame element model (PISA3D)—were explored for their effectiveness in predicting the cyclic behavior of the SPD test specimens (Tsai et al., 2018). The Abaqus model, shown in Figures 4(a) and 4(b), was able to represent the cyclic behavior, including strength degradation, quite well, even without simulation of the IC web fractures.

The PISA3D model included five beam-column elements, with one representing the IC, two representing EJ without the T-shaped stiffeners, and two representing the portions of the EJ with the T-shaped stiffeners, as shown in Figure 4(c). The beam-column elements were capable of forming shear and/or bending plastic hinges at each end. The IC segment used a two-surface plasticity material model, combining isotropic and kinematic hardening. No fracture or strength degradation was simulated. The PISA3D model was able to reasonably represent the force-deformation response of both specimens up to 4% interstory drift, as shown in Figure 4(d). Additional details of the numerical models can be found in Tsai et al. (2018).

NONLINEAR RESPONSE ANALYSES OF SPD-MRF MODELS

The proposed seismic design procedures were further validated through nonlinear response analyses of a prototype SPD-MRF building. Abaqus and PISA3D models were subjected to cyclic push-pull deformations and simulated ground motions. Some results from the PISA3D models will be presented here.

Prototype Building and SPD-MRF Models

The prototype office building was designed for a location in Chiayi City, Taiwan, with a design peak ground acceleration

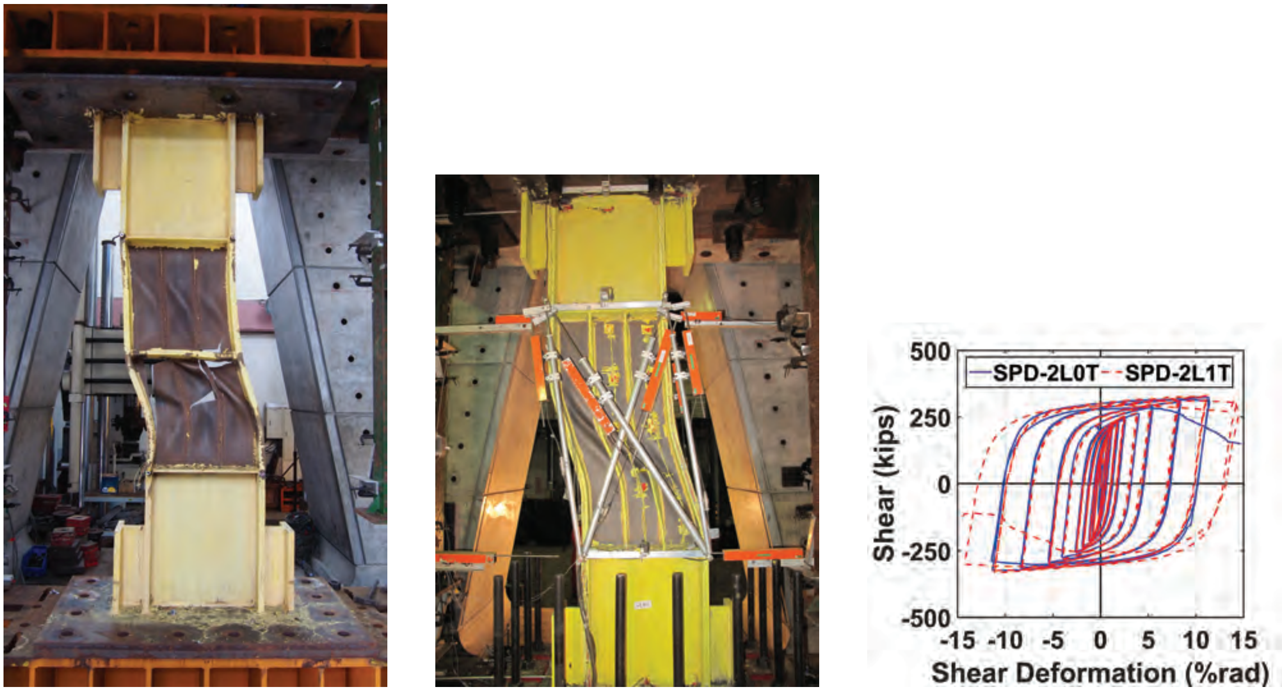

(a) (b) (c)

Fig. 3. (a) Specimen SPD-2L1T at end of test; (b) specimen SPD-2L0T at first cycle of 0.05-rad drift; (c) shear vs. inelastic core rotation.

of 0.33*g*. The six-story building is approximately 177 ft × 108 ft in plan and 68 ft tall, with longitudinal MRF frames and transverse SPD-MRF frames at the perimeter as shown in Figure 5(a). The transverse frames each contain two bays with SPD located at mid-span of 39.4 ft beams as shown in Figure 5(b).

The SPD-MRF were designed with SN400B steel for the IC and SN490B steel for the SPD flanges, EJ webs, and all beams and columns. The 8.53-ft-tall SPDs ranged from approximately 2 ft to 3 ft in depth. IC thicknesses and heights ranged from 0.157 in. to 0.315 in. and 35.4 in. to 70.9 in., respectively. Capacity design procedures were followed to prevent shear or flexural yielding in the boundary beams. Capacity design of SPD-to-beam panel zones resulted in doubler plates at all stories. Additional prototype SPD-MRF design details can be found in Tsai et al. (2018).

The PISA3D model utilized frame elements for all members and centerline dimensions. The prototype building

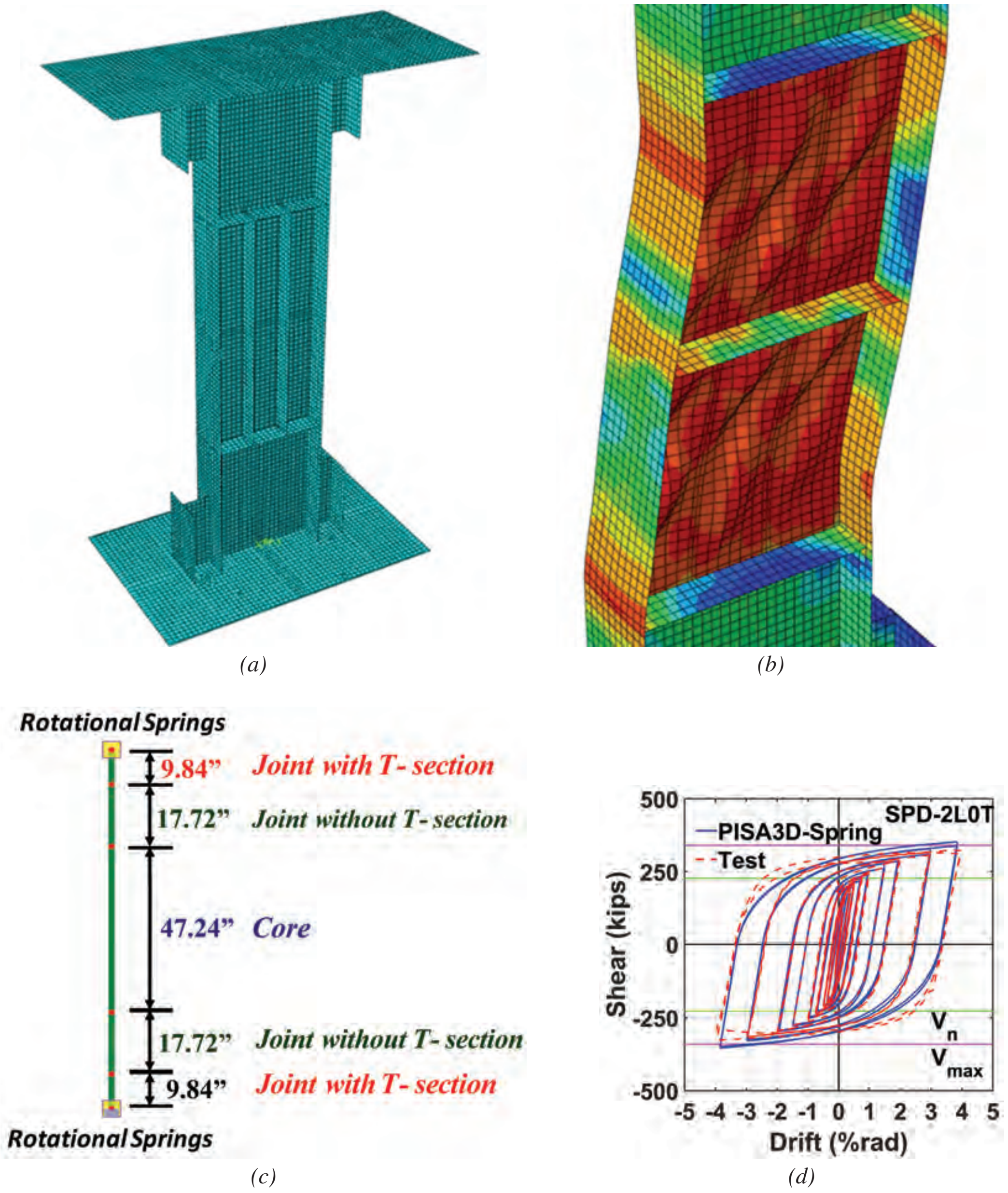

(a) (b)

(c) (d)

Fig. 4. (a) Abaqus model for specimen SPD-2L1T; (b) deformed shape of Abaqus model; (c) PISA3D model; (d) experimental and PISA3D shear vs. interstory drift for SPD-2L0T.

SPD-to-beam connections did not require T-shaped stiffeners (used to anchor the test specimens to the test set-up), so the SPD models had three elements instead of five. Panel zones were modeled with zero-length joint elements. Rigid offsets were used at beam-column joints. The two-surface plasticity material model was used for the IC elements, and a bilinear kinematic hardening material model was used for all other elements. Additional modeling details, including comparisons with an Abaqus model and cyclic push-pull results, can be found in Tsai et al. (2018).

Seismic Performance of Prototype Building

Nonlinear dynamic time-history analyses were conducted for 240 ground accelerations, evenly distributed across three hazard levels. The ground motions were scaled to spectral accelerations corresponding to the fundamental period of the prototype building in the transverse, SPD-MRF direction. The first 80 ground motions were scaled to the maximum considered earthquake (MCE), the next 80 motions to the design basis earthquake (DBE), and the last 80 to the service level earthquake (SLE).

The primary parameters of interest were the IC rotations, the system overstrength, the maximum roof drift, and the cumulative plastic deformations in the SPD. For IC deformations, the mean, maximum IC rotation was 0.041 rad for the MCE, and the maximum IC rotation never exceeded the 0.11 rad of deformation capacity measured in the SPD tests. Mean plus one standard deviation gave 0.055-rad IC rotation for the MCE. Mean, cumulative plastic deformations (CPD) were also significantly lower than the measured CPD capacities of the SPD. The mean system overstrength was 2.66 for the MCE, 2.46 for the DBE, and 1.34 for the SLE. Mean plus one standard deviation results for maximum roof drift were 1.43%, 1.20% and 0.51% for the MCE, DBE and SLE, respectively, as shown in Figure 6. The design drift limit was satisfied for all DBE ground motions. Analysis results are described in more detail in Tsai et al. (2018).

Additional Design Considerations

The SPD study included more investigation into the T-shaped stiffeners, an equivalent one-element model, and proportioning for stiffness. Analysis of Abaqus models confirmed that the capacity design methods proposed for the EJ are valid for SPD without T-shaped stiffeners. To facilitate use of a simple one-element model that is equivalent to the three-element model, equations were developed for equivalent cross-sectional properties, effective yield stress, and effective post-yield stiffness. A parametric study was also conducted to investigate effects of the IC height ratio and cross-sectional properties on the elastic and post-yield stiffness of the SPD. Methods focused on increasing SPD stiffness without altering the strength of the SPD. Results showed that decreasing the height of the IC and increasing the EJ web thickness were both effective in increasing SPD stiffness.

SUMMARY AND FUTURE WORK

Research has expanded the knowledge base on steel panel dampers beyond behavior, design and detailing of the inelastic core (IC). The work by Tsai et al. (2018) has provided new information on the seismic performance of SPD-MRF, as well as comprehensive guidelines for seismic design of the three-segment SPDs and SPD-MRF. This has been accomplished through testing of two full-scale SPD specimens, design of a six-story prototype SPD-MRF building, and numerical simulations using Abaqus and PISA3D. Seismic design procedures include design of the IC segment and

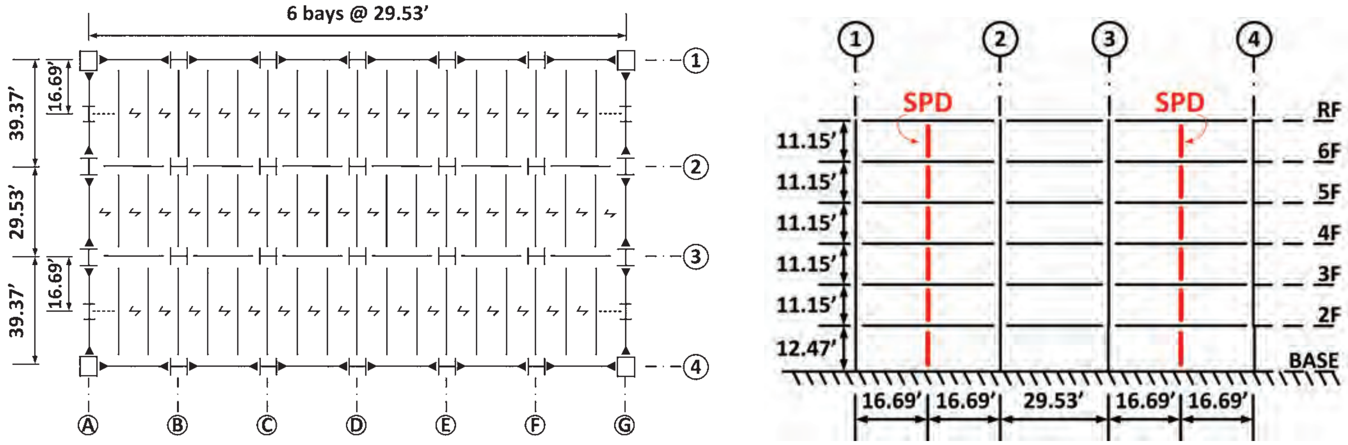

(a) (b)

Fig. 5. (a) Floor framing plan; (b) transverse frame elevation.

capacity design methods (CDM) for the elastic joint (EJ) segments, boundary beams, and the SPD-to-beam panel zones. Additional contributions include a three-segment SPD model, an equivalent one-element model, and guidelines for adjusting properties to achieve higher stiffness without affecting the strength of the SPD.

The decoupled SPD stiffness and strength offers some unique opportunities for design optimization of SPD-MRF. Research is under way on optimization of the stiffness of the SPD and the supporting beams. The studies include investigation into SPD locations with the frame and different options for SPD-MRF configurations.

ACKNOWLEDGMENTS

Special thanks to Dr. Keh-Chyuan Tsai for his many contributions to this article and to Dr. Ching-Yi Tsai, postdoctoral fellow, and former master's students Chung-Hsiang Hsu and Pu-Yuan Chin for creating the figures. Funding for the research was provided by the National Center for Research on Earthquake Engineering (NCREE) and Taiwan's Ministry of Science and Technology, Grant 105-2625-M-002-002. Any opinions, findings, conclusions and recommendations presented in this paper are those of the researchers and do not necessarily reflect the views of the sponsor.

REFERENCES

AISC (2016), *Seismic Provisions for Structural Steel Buildings,* ANSI/AISC 341-16, American Institute of Steel Construction, Chicago, IL.

AISC (2018), *Educator Awards*, American Institute of Steel Construction, www.aisc.org/education/university-programs/educator-awards/#14547, accessed May 9, 2018.

Chen, Z., Ge, H. and Usami, T. (2006), "Hysteretic Model of Stiffened Shear Panel Dampers," *Journal of Structural Engineering,* Vol. 132, No. 3, pp. 478–483. doi: 10.1061/(ASCE)0733-9445(2006)132:3(478).

Lee, J., Kang, H. and Kim, J. (2017), "Seismic Performance of Steel Plate Slit-Friction Dampers," *Journal of Constructional Steel Research,* Vol. 136, pp. 128–139. http://dx.doi.org/10.1016/j.jcsr.2017.05.005.

Lee, J. and Kim, J. (2017), "Development of Box-Shaped Steel Slit Dampers for Seismic Retrofit of Building Structures," *Engineering Structures,* Vol. 150, pp. 934–946. http://dx.doi.org/10.1016/j.engstruct.2017.07.082.

Li, C.H., Wu, C.C., Tsai, K.C., Lin, K.C. and Juang, S.J. (2018), "Fracture Behavior of Electro-Slab Welded Joint in Steel Beam-to-Box Column Connection," *Eleventh U.S. National Conference on Earthquake Engineering,* Los Angeles, CA, June 25–29, 11 pages.

Liu, Y., Aoki, T., Takaku, T. & Fukumoto, Y. (2007), "Cyclic Loading Tests of Shear Panel Damper Made of Low Yield Steel," *Journal of Construction Engineering,* Vol. 53A (in Japanese).

Martinez, C.A. and Curadelli, O. (2017), "Testing and Performance of a New Friction Damper for Seismic Vibration Control," *Journal of Sound and Vibration,* Vol. 399, pp. 60–74. http://dx.doi.org/10.1016/j.jsv.2017.03.022.

NCREE (2018), *AISC/NCREE Special Concentrically Braced Frame Test.* http://exp.ncree.org/scbf/index.html, accessed May 22, 2018.

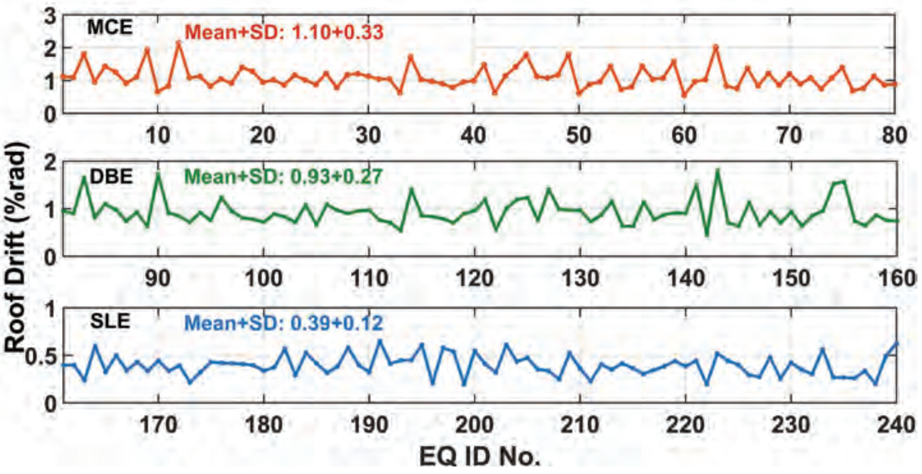

Fig. 6. Nonlinear time-history analysis results for maximum roof drift for each earthquake (EQ) ground motion.

Otani, M., Inai, E., Matsuura, T. and Ito, Y. (2001), "Structural Performance of Shear Panel Dampers Using Low Yield Strength Steel, Parts 1–3," *Abstract Volume of Technical Papers of Annual Meeting, Architectural Institute of Japan* (in Japanese).

Tanaka, K. and Sasaki, Y. (2000), "Hysteretic Performance of Shear Panel Dampers of Ultra Low-Yield Strength Steel for Seismic Response Control of Buildings," *Proceedings of the 12th World Conference on Earthquake Engineering,* WCEE, New Zealand.

Tsai, K.-C., Hsu, C.-H., Li, C.-H. and Chin, P.-Y. (2018), "Experimental and Analytical Investigations of Steel Panel Dampers for Seismic Applications in Steel Moment Frames," *Earthquake Engineering and Structural Dynamics,* Vol. 47, No. 6, pp. 1,367–1,588. http://dx.doi.org/10.1002/eqe.3023.

Tsai, K.-C., Lin, K.-C., Juang, S.-J., Li, C.-H. and Lin, C.-H. (2015), "Research and Practice on Seismic Design of Welded Steel Beam-to-Box Column Moment Connections in Taiwan," *Symposium on Future Development of Seismic Design,* Hong Kong, February 13, 16 pages.

Tsai, K.-C., Wang, H.-Y., Chen, C.-H., Liu, G.-Y. and Wang, K.-J. (2001), "Substructure Pseudo Dynamic Performance of Hybrid Steel Shear Panels," *Steel Structures,* Vol. 1, No. 2, pp. 95–104.

Wang, G., Wang, Y., Yuan, J., Yang, Y. and Wang, D. (2017), "Modeling and Experimental Investigation of a Novel Arc-Surfaced Frictional Damper," *Journal of Sound and Vibration,* Vol. 389, pp. 89–100. http://dx.doi.org/10.1016/j.jsv.2016.11.019.

Guide for Authors

Scope

Engineering Journal is dedicated to the improvement and advancement of steel construction. Its pages are open to all who wish to report on new developments or techniques in steel design, research, the design and/or construction of new projects, steel fabrication methods, or new products of significance to the uses of steel in construction. Only original papers should be submitted.

General

Papers intended for publication should be submitted by email to Margaret Matthew, Editor, at matthew@aisc.org.

The articles published in the *Engineering Journal* undergo peer review before publication for (1) originality of contribution; (2) technical value to the steel construction community; (3) proper credit to others working in the same area; (4) prior publication of the material; and (5) justification of the conclusion based on the report.

All papers within the scope outlined above will be reviewed by engineers selected from among AISC, industry, design firms, and universities. The standard review process includes outside review by an average of three reviewers, who are experts in their respective technical area, and volunteers in the program. Papers not accepted will not be returned to the author. Published papers become the property of the American Institute of Steel Construction and are protected by appropriate copyrights. No proofs will be sent to authors. Each author receives three copies of the issue in which his contribution appears.

Manuscripts

Manuscripts must be provided in Microsoft Word format. Include a PDF with your submittal so we may verify fonts, equations and figures. View our complete author guidelines at **www.aisc.org/ej**.

Smarter. Stronger. Steel.

American Institute of Steel Construction
130 E Randolph St, Ste 2000, Chicago, IL 60601
312.670.2400 | www.aisc.org